

https://dspace.org/

Solar cell device simulations from ab initio data and the implementation of efficiency enhancing techniques

Mokgosi, Itumeleng Siphiwe

2018

https://hdl.handle.net/10539/26915

Mokgosi, Itumeleng Siphiwe (2018) Solar cell device simulations from ab initio data and the implementation of efficiency enhancing techniques, University of the Witwatersrand, Johannesburg, https://hdl.handle.net/10539/26915

Downloaded from a DSpace repository. https://dspace.org/

Solar cell device simulations from ab initio data and the implementation of efficiency enhancing techniques.



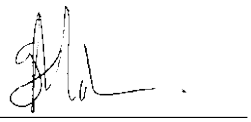
Master of Science dissertation

Itumeleng Mokgosi (542166)

School of Physics
Supervisor: Prof. Alex Quandt
Co-Supervisor: Dr. Robert Warmbier

Declaration

I hereby declare that this dissertation is my own original work and has not been submitted before to any institution for assessment purposes. Further, I have acknowledged all sources used and have cited these in the reference section.



Itumeleng Mokgosi
24 October 2018

Abstract

With the global energy consumption at an all-time high and the demand for energy estimated to triple by 2050, renewable energy sources such as solar are pivotal in an addressing this global energy demand. Solar power generation by photovoltaic cells enjoys several advantages compared to other forms of electricity generation such as a reduced fossil fuel dependence, modularity, easy and flexible installation, and scalability.

The development of novel solar cells that offer increased efficiencies is an integral component of the process of addressing the global energy needs. Solar cell device simulations offer a cost-effective means to explore the impact of different material properties on the overall efficiency of the solar cell. The use of ab initio calculated material properties that serve as an import for the device simulations offers a means to easily study and estimate the typical solar cell efficiencies of different types of solar cells. The implementation of new light harnessing features, like frequency conversion layers or plasmonic nanoparticles, and the integration of these futures into existing device simulation codes serves as a useful tool that aids solar cell development.

This work explores the theoretical and numerical background for the simulation of solar cell devices. A brief explanation of how ab initio calculated parameters can be used, together with the implementation of frequency conversion techniques in existing simulation codes is given. It is shown that the solar cell performance parameters can be well approximated using ab intio parameters. Also, the positive effect of frequency conversion techniques is demonstrated with examples of how this tool can be implemented in existing solar cell device simulation codes. The approaches discussed in this work can serve as a good framework for the modeling of novel solar cell devices.

Acknowledgements

To undertake studies of any magnitude is not possible without the assistance of individuals and organisations that devote their time and resources to assist you in any way they can. I would like to thank my supervisor, Prof Alex Quandt, and my co-supervisor Dr Robert Warmbier, for their relentless guidance, advice and encouragement that they provided throughout my tenure as their student. I have been very fortunate to have supervisors who cared so much about my work, and availed themselves promptly for any of queries.

To the academic staff of the Wits University Physics department and fellow students, I am deeply honoured to have had all those enlightening conversations over tea about our various research topics, which served as a reminder about why we do what we do making the struggle bearable.

I am also sincerely grateful to the generous financial support that I received from the Centre of Excellence in Strong Materials(CoE-SM) for the tenure of my project. The generous financial support made it possible for me to produce work that has been presented at various international conferences and resulted in several publications.

To my family and close friends, I am entirely grateful to have you in my life and appreciate the support you give in my pursuit to achieve my dreams. This work is dedicated to all of you.

Contents

Declaration **1**

1 Introduction **1**
1.1 Background 1
1.1.1 Solar resource 2
1.1.2 Energy conversion 4
1.1.3 Solar cell devices 4
1.1.4 I-V curve and related output parameters explained . . 7
1.1.5 Fill Factor and Efficiency 8
1.1.6 Device Simulations 10
1.2 Hypothesis and questions 11
1.3 Aims 11
1.4 Objectives 11
1.5 Methodology 12
1.6 Report outline 12

2 Fundamental device physics **13**
2.1 Properties of Semiconductors 13
2.1.1 Semiconductor band structure 14
2.1.2 Equilibrium carrier concentrations 16
2.1.3 Light absorption 20
2.2 Carrier generation 24
2.3 Recombination 25
2.4 Carrier transport 29
2.5 Semiconductor device equations 32
2.6 Minority-carrier diffusion equation 33
2.7 Summary 34

3 Solar cell operation and performance **35**
3.0.1 Solar cell parameters 35
3.1 Summary 36

4 Simulation software **37**
4.1 AMPS1D . . . 37
4.2 WxAMPS . . . 39
4.3 PC1D . . . 41
4.4 SCAPS . . . 43
4.5 GPVDM . . . 44
4.6 Chapter summary . . . 45

5 Device simulations **46**
5.0.1 Simulation of the silicon based P-N junction . . . 53
5.0.2 Discussion . . . 58
5.1 Summary . . . 60

6 Frequency conversion **61**
6.1 Up-conversion . . . 61
6.2 Down-conversion . . . 62
6.2.1 The general rate equation model . . . 63
6.2.2 Photon absorption and emission . . . 63
6.2.3 Generation rate and photocurrent density . . . 64
6.3 Up-conversion results . . . 65
6.3.1 Energy scheme and rate equations for Er^{3+} co-doped with Yb^{3+} . . . 65
6.3.2 Results . . . 67
6.3.3 Energy scheme and rate equations for trivalent thulium (Tm^{3+}) system . . . 70
6.3.4 Results . . . 71
6.3.5 Discussion . . . 74
6.4 Summary . . . 75

7 Conclusions and future work **76**
7.1 Conclusions . . . 76
7.2 Future work . . . 76

List of Figures

1.1 Available solar irradiation 3
1.2 Semiconductor energy band diagram (equilibrium) 5
1.3 Semiconductor energy band diagram (non-equilibrium) 5
1.4 Solar cell device 6
1.5 Dark current I-V curve representation 8
1.6 Illumination I-V curve representation 8
1.7 First quadrant representation of I-V curve 8
1.8 Diagram showing solar cell efficiency and fill factor 9
1.9 1d layer setting for device simulations 10
1.10 Typical I-V output for P-N junction solar cell 10

2.1 Band diagram illustration at T>0 K in direct bandgap semiconductors 15
2.2 The Fermi function at various temperatures 17
2.3 Photon absorption in a direct bandgap semiconductor 20
2.4 Photon absorption in an indirect bandgap semiconductor . . . 21
2.5 Absorption coefficient given as a function of photon energy for indirect(Si) and direct(GaAs) bandgap materials 23
2.6 Recombination processes in solar cells 25
2.7 Mobilites for silicon at 300 K 30

4.1 Main Screenshot for AMPS1D 37
4.2 Sample Si simulation using AMPS1D 39
4.3 Main Screenshot for WxAMPS 39
4.4 Material parameters screenshot for WxAMPS 40
4.5 Sample simulation using WxAMPS 41
4.6 Main screenshot for PC1D 41
4.7 Sample simulation using PC1D 42
4.8 Main screenshot for SCAPS 43
4.9 Sample simulation using SCAPS 44
4.10 Main screenshot for GPVDM 44
4.11 Sample simulation using GPVDM 45

5.1 DFT-PBE band structure of Si. 48
5.2 Absorption coefficient of Si calculated using BSE as compared to experimental results [1]. 50
5.3 P-N junction simulation using experimental data 55
5.4 P-N junction simulation using ab initio data 55
5.5 IV curve for light doping case 57
5.6 IV curve for the moderate doping case 58
5.7 IV curve for the heavy doping case 58

6.1 Energy scheme of Er^{3+} co-doped with Yb^{3+} 65
6.2 Simulation result without UC (Er/Yb system) 69
6.3 Simulation result with UC (Er/Yb system) 70
6.4 Energy scheme of Tm^{3+} 71
6.5 Simulation result without UC (Th^{3+} system) 73
6.6 Simulation result with UC (Tm^{3+} system) 73

List of Tables

5.1 Ambient properties for simulations 47
5.2 Table of absorption data and other properties for Si (ab initio) 52
5.3 Properties of silicon at 300 K 53

6.1 Parameters used for the Er/Yb system calculations 67
6.2 Population densities of the energy levels (Er/Yb system) . . . 68
6.3 Summary of UC results (Er/Yb system) 70
6.4 Parameters used for Tm^{3+} rate equations calculations 72
6.5 Population densities of the energy levels for Tm^{3+} 72
6.6 Summary of UC results (Thulium system) 74

Chapter 1

Introduction

1.1 Background

A substantial proportion of the world's electricity demand is currently met by using continuously depleting fossil fuels such as natural gas, coal and oil. Apart from their limited availability due to their non-renewable nature, these conventional energy sources face a lot of challenges such as rising commodity prices, supply security concerns from imports from a small number of countries with fossil fuel supplies, and an increasing environmental concern about the climate change risks that are coupled with fossil fuel power generation[2]. The forever increasing world energy consumption is estimated to triple by 2050 with the continued increase in world population, coupled with the continuous development of emerging market countries[3]. Renewable energy resources are pivotal in addressing some of these concerns. The development of novel photovoltaic technologies is an integral component of the solution for the world‘s energy needs, and modeling of these device is an integral component of the research and development.

Solar power generation by photovoltaic cells (solar cells) enjoys many benefits compared to other forms of electricity generation such as reduced fossil fuel dependence, modularity, easy and flexible installation, and scalability. Solar cell are devices that convert light energy from the sun into useful electrical energy[4]. These devices make use of the photovoltaic effect to achieve this.

The first occurrence of a true solar cell dates to 1883, when Charles Fritts constructed one by using junctions formed by coating selenium with a thin layer of gold[5]. The advent of modern photovoltaic technology came in 1954,

when 3 researchers namely C. Fuller, D. Chapin, and G. Pearson developed the silicon based PV cell at Bell Telephone Laboratories in the US. This was the the first ever device that could convert enough of the sun's energy into usable power. This solar cell delivered an efficiency of about 4%[3]. These types of solar cells reached an efficiency of 14% by 1960. Research and development in photovoltaics was driven by the boom of space exploration during that era. In the 1970's, during the first oil crisis, large solar companies were established in japan and the US paving the way for a golden age for PV technology. Majority of the production was driven by electricity demand in off-grid areas. Electricity production from PV peaked at 9.3 MW by 1982 and by the end of 2002, the number of PV manufacturing companies sat at around 80%[3].

The sole energy source of solar cells is photons emitted from the sun. To ensure that the solar resource is sufficiently exploited, a thorough understanding of solar cells functionality, their overall performance, and how these devices can be improved is of utmost importance. Solar cell device simulations from available numerical and experimental data offer a means of exploring different types of solar cells in the pursuit to develop more novel and efficient solar cells. In the quest to reduce production costs and increase the power conversion efficiency of the solar cell, computer based modeling of solar cell devices helps pave the way in producing cost effective and highly competitive solar cells.

1.1.1 Solar resource

The energy that we receive from the sun is a very important form of energy for life on earth. The sun is a black body that emits electromagnetic radiation with a spectral distribution that is determined by the sun's temperature. The spectral radiation distribution that's emitted is given by the Plank's radiation law[6]. The wavelengths observed in the Sun's electromagnetic spectrum span over 10 orders of magnitude: from the shortest gamma rays and X-rays to radio waves longer than 1m. However, most of radiative energy reaching our planet is situated in the ultraviolet ($\sim 8\%$), visible ($\sim 40\%$) and infrared ($\sim 52\%$) regions of the solar spectrum[7].

Irradiance (insolation) is the incident flux of radiant energy in a given area and it is measured in watts per square meter. The radiant power per unit area perpendicular to the direction of the sun outside the earth's atmosphere is called the solar constant, or air mass zero (AM0). The widely accepted

value of the solar constant is 1.353 kW/m^2[6].

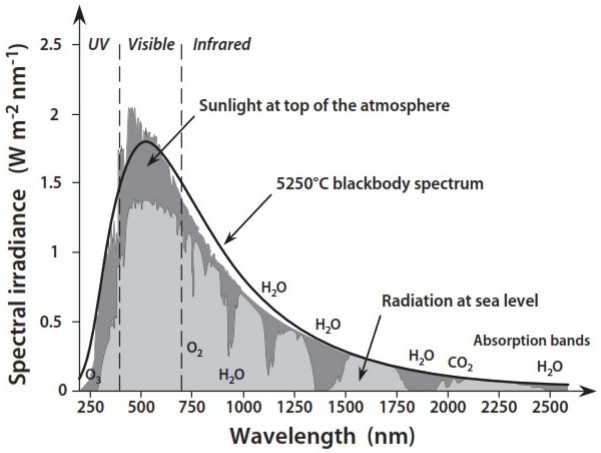


Figure 1.1: Available solar irradiation
(sourced from [7])

Figure 1.1 shows the solar irradiance as a function of wavelength[7]. A knowledge of the solar energy distribution is important in solar cell research because different solar cells respond differently to different wavelengths of light.

As sunlight passes through the earth's atmosphere, it is attenuated by at least 30% due to Rayleigh scattering, scattering by aerosols and dust particles, and atmospheric absorption from the atmospheric gases.

Since the amount of attenuation is not constant, the crucial parameter that helps us to determine the total incident power under clear weather conditions is the light path length through the atmosphere. The ratio of any path length to its lowest value is called the optical air mass(AM). When the sun is at an angle θ to the overhead, the AM is[6]

$$Airmass(AM) = \frac{1}{cos\theta}. \tag{1.1}$$

The more universally used spectrum is the AM1.5 spectrum. It entails a power flux of about 970 W/m^2 which is generally rounded to give 1000 W/m^2, a quantity commonly termed "one sun"[7].

1.1.2 Energy conversion

In photovoltiac energy conversion, there are essentially 4 steps involved[8].

1. A process that involves the absorption of light which results in a transition in a material from an electronic ground state to an excited state[**Absorption**].
2. The excited state is then converted into a free negative (electron) and free positive charge (hole) carrier pair[**Generation**].
3. A transport mechanism which acts as a discriminator and causes the negative and positive charge carriers to move in opposite directions. The contacts that these charge carriers drift to are called cathode and anode, respectively[**Separation**].
4. Recombination of charge carriers at the anode, returning the absorber to its ground state[**Recombination**].

1.1.3 Solar cell devices

Semiconductors

All the above mentioned photovoltaic energy conversion steps take place in the semiconductor material. Therefore, the material properties of semiconductors are central in the transport properties of solar cell devices. A semiconductor in equilibrium has a basic band structure given in figure 1.2. E_V is called the valence band edge, which is the highest allowed energy of the valence band. E_C is called the conduction band edge, which is the lowest allowed energy in the conduction band. The difference between E_C and E_V is called the band gap (E_G). E_F denotes the Fermi energy, which is the electrochemical potential of all the electrons in the material[9]. Figure 1.3 below shows a schematic of a semiconductor energy diagram under illumination (non-equilibrium). In this non-equilibrium states, two quasi-Fermi energy levels are used to describe the occupation of states by the electrons and the holes. E_{FC} is the quasi-Fermi energy for the electrons and it describes the occupation of the states in the conduction band with electrons.

E_{FV} is the quasi-Fermi energy for holes and it describes the states which are filled in the valence band with holes. The difference between E_{FC} and E_{FV} is called the electrochemical energy(μ_{eh}) of the generated electron-hole pairs[9].

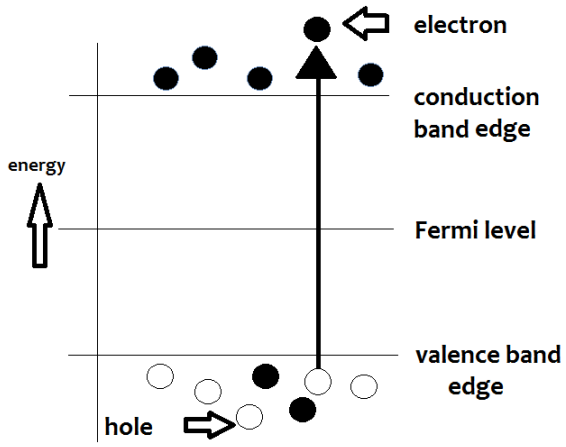


Figure 1.2: Semiconductor energy band diagram (equilibrium)

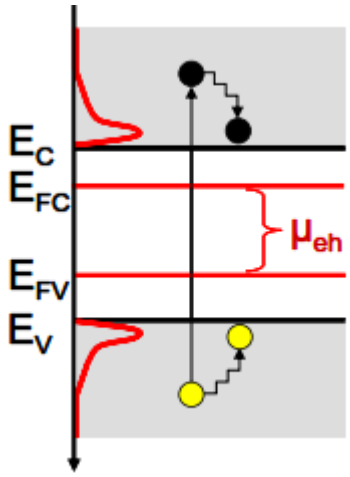


Figure 1.3: Semiconductor energy band diagram (non-equilibrium)
(sourced from [10])

P-N junction

A typical solar cell device is simply a classical P-N junction with back and front contacts. P-N junctions are made by joining a n-type semiconductor layer and a semiconductor p-type layer. The n-type layer has a high electron concentration due to the introduction of dopants with extra electrons, and the p-type layer has a high hole concentration due to the introduction of dopants with extra holes. The excess in the respective particles in each layer causes electron diffusion from the n-type side to the p-type side, and hole diffusion from the p-type side to the n-type side. The diffusion results in recombinations with dopants, and thus the creation of localized charges. An electric field forms between the exposed positive and negative charges in the n-type material and the p-type material, respectively. This resulting electric field sweeps out free carriers in that region at the interface between the n-type and the p-type layer. This region is called the depletion region (junction region)[11]. A diagram depicting a solar cell is given in figure 1.4.

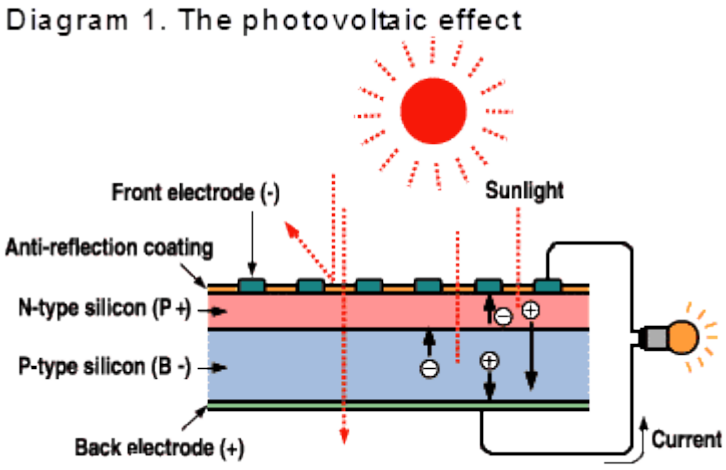


Figure 1.4: Solar cell device
(sourced from [12])

1.1.4 I-V curve and related output parameters explained

The IV curve and the solar cell efficiency are the important outputs that are obtained from the device simulations. This section explains the physics behind the I-V curve and how the solar cell efficiency is determined.

I-V curve

The solar cell I-V curve is the superposition of the I-V curve of the solar cell diode in the dark with an additional light-generated current[11]. The generated current from the light essentially shifts the I-V curve of the Shockley diode equation down such that it is possible to extract power from the diode. Illuminating the solar cell adds free charge carriers to the normal "dark" currents and the diode law becomes[6]:

$$I = I_s \left[exp\left(\frac{qV}{nkT}\right) - 1 \right] - I_L \tag{1.2}$$

I_L is the light generated current. I_s is the saturation current (dark current). V is the voltage across the diode, q is the electron charge, and n is the ideality factor that accounts for the imperfect junctions. It is convention to give the first quadrant representation of the I-V curve. Equation 1.2 is then modified to

$$I = I_L - I_s \left[exp\left(\frac{qV}{nkT}\right) - 1 \right]. \tag{1.3}$$

The images below give a visual illustration of the diode equation I-V curve without illumination, with illumination, and the first quadrant representation, respectively[13].

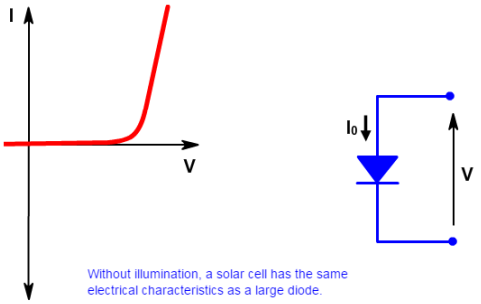


Figure 1.5: Dark current I-V curve representation
(sourced from [13])

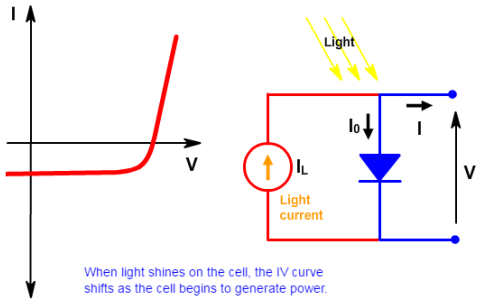


Figure 1.6: Illumination I-V curve representation
(Sourced from [13])

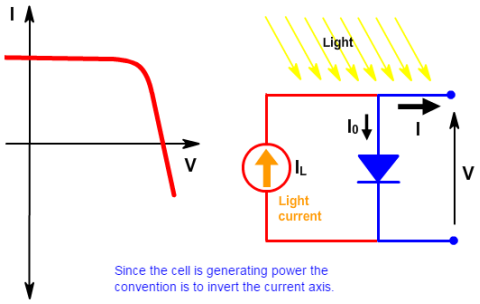


Figure 1.7: First quadrant representation of I-V curve
(Sourced from [13])

1.1.5 Fill Factor and Efficiency

The fill factor(FF) of the solar cell is defined as the ratio of the maximum power from the solar cell to the product of the open circuit voltage(V_{oc}) and

the short circuit current (I_{sc}). V_{oc} is the maximum voltage available from a solar cell, which is found at at 0 current. I_{sc} is the current through the cell when the voltage across the solar cell is 0. FF is given by[14]:

$$FF = \frac{V_{mp} \times I_{mp}}{V_{oc} \times I_{sc}} \tag{1.4}$$

V_{mp} and I_{mp} are the voltage and the current values at the maximum power point.

The power conversion efficiency can be defined as the electrical power coming out of the cell into a matched load, divided by the incident solar power falling on the solar cell. It is given by[15]:

$$\eta = \frac{V_{oc} I_{sc} FF}{P_{in}} \tag{1.5}$$

P_{in} is the the input power from the sun. A diagram showing the above mentioned parameters is given below in figure 1.8.

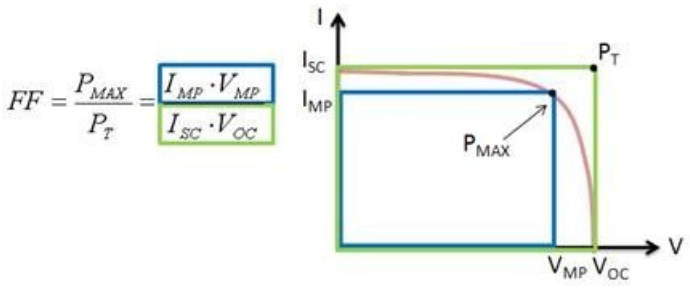


Figure 1.8: Diagram showing solar cell efficiency and fill factor

1.1.6 Device Simulations

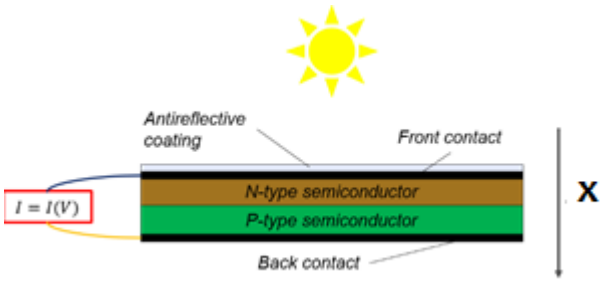


Figure 1.9: 1d layer setting for device simulations
(courtesy of Prof. A. Quandt)

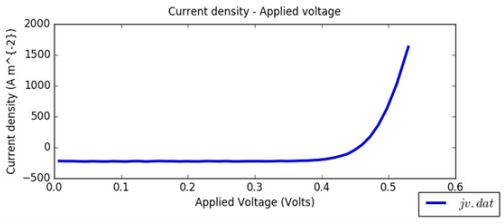


Figure 1.10: Typical I-V output for P-N junction solar cell

In the device simulations, there are three governing equations which are mostly one dimensional and are solved numerically. These are namely the Poisson equation, the continuity equation for the free holes, and the continuity equation for the free electrons. The physical properties are functions of the x-direction perpendicular to the various layers of the device as illustrated in 1.9. The task of determining transport characteristics is simply a task of computing these 3 coupled non-linear differential equations with the aid of appropriate boundary conditions[16]. The main properties obtained by the device simulation program are the I-V characteristics for the dark and illumination conditions, which can be easily compared against known data. These I-V characteristics determine the overall efficiency of solar cell. A typical I-V curve from a device simulation using the GPVDM software package is given in figure 1.10[17].

1.2 Hypothesis and questions

With the rise in the development of novel and improved solar cell devices, an affordable and reliable means to explore and test different types of solar cell devices is a crucial component in realising the desired goal of reaching efficiencies much greater than the postulated 34% by Shockley and Queisser for a single junction cell without concentration[15]. Device simulations using both experimental and numerical data offer a possible means to probe the properties of solar cell devices, and implement and study different techniques that can enhance the performance of such devices. The usage of such simulations, can eliminate the squandering of enormous sums of money on unnecessary prototype development. As such, it is important to probe the possibility of using such simulations with a thorough understanding of their merits and limitations.

1.3 Aims

The overall aim of this research project is to simulate solar cell devices from ab initio and experimental data using an appropriate computer program, and to study the effects of various device parameters on the overall efficiency of the solar cell. The implementation of light harvesting in the UV and infrared such as up conversion and down conversion in solar cell device simulations shall also be explored.

1.4 Objectives

1. Learn and understand the basics of solar cell device physics, and use the acquired knowledge to produce meaningful device simulations.

2. Learn and understand how device simulation programs work and what meaningful information can be obtained from the results.

3. Explore meaningful ways of improving solar cell performance using the generated simulations.

4. Investigate the effect of both optical and electronic material properties on the solar cell performance.

5. Compare the ab initio data and the corresponding device simulations to devices modeled from data obtained in literature.

6. Explore the possibility of implementing efficiency enhancing techniques within the device simulations by adding functionality to the existing code.

1.5 Methodology

A thorough search and analysis of the available device simulation programs such as AMPS-1D, GPVDM and SCALPS shall be done, and a comparison of their merits and shortcomings shall be completed. Typical device simulations shall be done using the available numerical and experimental data. The possibility of implementing efficiency enhancing techniques such as up and down conversion shall be studied and an illustration of how this can be implemented in the modelling of devices shall be explored.

1.6 Report outline

First, an overview of the fundamental physical principles that govern the functioning of solar cell devices is given in chapter 2. All the crucial performance parameters that are used in distinguishing solar cell devices are highlighted thereafter in chapter 3. We then explore the different solar cell device simulation software packages that are available with an emphasis on their merits and shortcomings in the chapter that follows. Chapter 5 gives an outline of how ab initio data is obtained and how it is used in the device simulations. A comparison of the ab initio data-based and an experimental data-based simulation is done. Frequency conversion is explored in chapter 6 and the report conclusion and the future work section is given thereafter in chapter 7.

Chapter 2

Fundamental device physics

This chapter gives an overview of the physical principles and properties that are crucial for the understanding of solar cell modeling and device operation. The chapter canvasses through the fundamental properties of semiconductors that make them ideal for solar cell applications. Concepts underlying the typical semiconductor band structures found in solar cells, carrier generation, recombination and transport are reviewed.

2.1 Properties of Semiconductors

Familiarity with the fundamentals of solid state physics is crucial in understanding the operation of semiconductor solar cells. Many different semiconductor materials such as Gallium arsenide (GaAs), silicon (Si) which is either crystalline, amorphous or polycrystalline in nature, GaInP, CdTe, etc, can be used for the fabrication of different types of solar cells. The choice of a specific material depends on the cells' solar absorption characteristics and the cost of fabrication. Due to silicon having desirable absorption characteristics and well-established fabrication technology due to the electronics industry, it has a pervasive usage in solar cell fabrication[18].

The semiconductor properties that underpin the performance and overall design of solar cell[19], and the resultant solar cell choice for a particular application are[20]:

1. The concentration of doping atoms. They can either be acceptor or donor atoms, where an electron is either accepted or donated by the atom, respectively.

2. The diffusion coefficient D and the mobility μ. These two characterise carrier transport within the device.

3. The diffusion length of the excess carriers and the carrier lifetime τ. These are central to carrier generation and recombination processes.

4. The bandgap energy E_g and the complex refractive index $n - \imath k$ that's related to the absorption coefficent α, which addresses the semiconductors ability to absorb photons.

2.1.1 Semiconductor band structure

Pure crystalline semiconductor materials are electronic grade [18]. This essentially means that they possess long range order. This orderly arrangement of atoms allows for the construction of the entire crystal structure by repeatedly stacking a small and defined volumes containing atoms. These small subsections that are used for the orderly construction of entire crystals are known as primitive cells[6]. Primitive cells contain all the necessary information to reconstruct the location of atoms in the crystal. Since some of these primitive cells may have awkward and irregular shapes, it is sometimes more convenient (since scientists prefer simplicity) to work with slightly larger cells which also contain all the necessary physical and chemical information called supercells. Atomic properties of the component elements of these materials, together with their unique periodicity, is what gives these semiconductor materials their very beneficial properties for use in solar cell applications.

To successfully utilise these electronic properties in solar cell modelling and development, it is important to understand them. As such, one can imagine a moving electron inside a semiconductor material which can be likened to a confined particle in a 3-dimensional box with a complicated interior structure. This approach is favoured and used in optical properties for quantum dot applications as done in [21]. The potential fields arising from the interaction with the atom's bound core electrons and nucleus and bound core electrons result in this complex interior structure. The overall behaviour of the electron in question can then be deduced from the electrons wavefunction ψ. This Bloch state ψ can simply be obtained by successfully computing the time-independent Schrodinger equation given by[18, 22]:

$$\nabla^2\psi + \frac{2m}{\hbar^2}\left[E - V(\vec{r})\right]\psi = 0. \tag{2.1}$$

Here, m is the electron mass, $\mathrm{E}(\vec{k})$ is the electron's energy, $V(\vec{r})$ is the system's lattice periodic potential. $\hbar$ is the Planck constant in its reduced form. The solution of 2.1 ultimately gives us the band structure $\mathrm{E}(\vec{k})$ of the semiconductor. It also shows that the electron's motion in the semiconductor crystal can be approximated by an electron in vacuum[18] if the electron mass m in equation 2.1 is exchanged with an "effective" mass m^* in the second law of motion by Newton[18, 23]. m^* essentially incorporates the effect of the periodic forces of the crystal atoms.

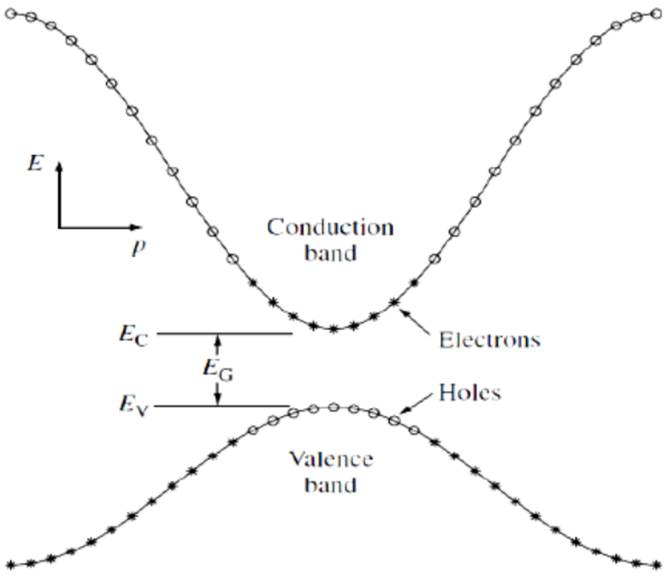


Figure 2.1: Band diagram illustration at T>0 K in direct bandgap semiconductors

(Sourced from [18])

Figure 2.1 illustrates a simple energy band structure. The energy states under the valence band are considered to be full, and the energy states above the conduction band are considered as empty. Only two bands are shown for the purpose of this illustration. The allowed energies are represented with respect to crystal momentum given by $\vec{p} = \hbar\vec{k}$[18], where $\vec{k}$ is the wavevector corresponding to ψ. The curvature of the bands define the effective mass which can essentially solved for by computing equation 2.2 . The empty valence band states near the top are considered as positively charged current carriers that are called holes. The conduction band curvature describes the effective mass for the electrons and the valence band curvature describes the effective mass for the holes. The effective mass is given by[18]

$$m^* = \left[\frac{d^2E}{dp^2}\right]^{-1} = \left[\frac{1}{\hbar^2}\frac{d^2E}{dk^2}\right]^{-1}. \tag{2.2}$$

The bandgap, E_G is the forbidden energy levels or energy gap that separates the valence-band edge(E_V) and the conduction-band edge(E_C), and it is one of the crucial material parameters for the selection and operation of solar cells [24]. The bandgap ultimately determines which of the photons from the sun shall contribute to the photocurrent.

When the valence band maximum is found at the same $\vec{k}$ with the minimum of the conduction band, the semiconductor is called a direct bandgap semiconductor. When the two are not at the same wavenumber, the semiconductor is called an indirect band gap semiconductor. The computation of the band structure, band gap and the electron and hole mobilities shall be discussed later in this work.

2.1.2 Equilibrium carrier concentrations

Semiconductor device operations depend on the charge carriers inside the semiconductor that drive electric currents. Therefore, to understand solar cell device operation, the number of charge carriers in the semiconductor device is a crucial parameter. The equilibrium condition means that the state of the system is unperturbed by any perturbing force such as external voltage, magnetic field, illumination and mechanical stress [25].

In order to determine the carrier concentrations for the holes and the electrons one has to know the density of allowed energy states for the valence and conduction band. The occupation function of these allowed states is also important. The density of states function, $g(E)$, denotes the number of allowed states per unit volume and energy[18, 19]. The $g(E)$ for the conduction band is approximately[26]

$$g_C(E) = \frac{m_n^*\sqrt{2m_n^*(E-E_C)}}{\pi^2\hbar^3} cm^{-3}eV^{-1}. \tag{2.3}$$

which corresponds to a parabolic band close to E_c. $g(E)$ for the valence band is[26]

$$g_V(E) = \frac{m_p^* \sqrt{2m_p^*(E_V - E)}}{\pi^2 \hbar^3} cm^{-3} eV^{-1}. \tag{2.4}$$

which corresponds to a parabolic band close to E_v. Here, the effective masses are represented by m_n^* and m_p^* for the electrons and holes, respectively.

The occupation function is a Fermi-Dirac distribution function, $f(E)$. It gives the ratio of the states which are filled to the available states at a given energy E, described by[25]

$$f(E) = \frac{1}{1 + e^{(E-E_F)/kT}}. \tag{2.5}$$

Here, the Boltzmann's constant is represented by k and E_F gives us the Fermi energy of the system.

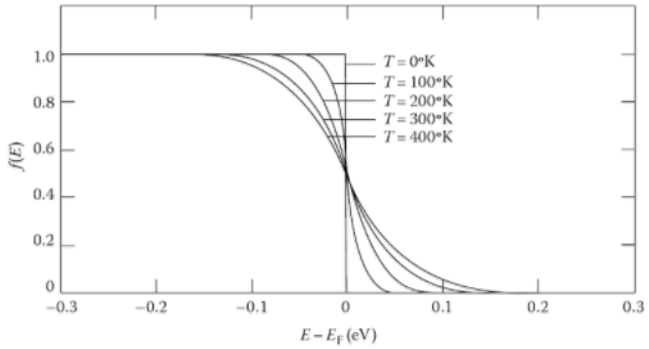


Figure 2.2: The Fermi function at various temperatures
(Sourced from [27])

The Fermi function is given in figure 2.2, which is shown as a function of temperature. It is a step function at 0 K[18], and the states below the Fermi energy are filled with electrons and those above the fermi energy are empty. At temperatures above zero Kelvin(T>0 K), thermal excitation leaves some of the states below the fermi energy unoccupied and some states above the Fermi energy filled with excited electrons.

Conduction band electrons and valence band holes are the carriers that contribute to charge transport. The total concentration (number per cm^3)

of each is given as[18]

$$n_0 = \int_{E_C}^{\infty} g_C(E) f(E) d(E) \tag{2.6}$$

$$p_0 = \int_{-\infty}^{E_V} g_V(E) \left[1 - f(E)\right] d(E), \tag{2.7}$$

where n_0 and p_0 give the electron and hole concentrations, respectively. Substituting $g(E)$ (2.3 and 2.4) and $f(E)$ (2.2) into equation 2.6 and 2.7 above yields the following expressions for nondegenerate semiconductors[28]

$$n_0 = N_C e^{(E_F - E_C)/kT} \quad for \quad E_C - E_F \geq 3kT \tag{2.8}$$

$$p_0 = N_V e^{(E_V - E_F)/kT} \quad for \quad E_F - E_V \geq 3kT. \tag{2.9}$$

Here, N_V and N_C are the effective densities of state (number of particles per unit volume) for the valence band and conduction band[29], respectively, given by[28]

$$N_C = 2\left(\frac{2\pi m_n^* kT}{h^2}\right)^{3/2} \tag{2.10}$$

$$N_V = 2\left(\frac{2\pi m_p^* kT}{h^2}\right)^{3/2}. \tag{2.11}$$

For an intrinsic (undoped) semiconductor that is in thermal equilibrium, $n_0 = p_0 = n_i$. n_i denotes the intrinsic carrier concentration[18]. n_i for the undoped system can be computed from [18]

$$p_0 n_0 = n_i^2 = N_C N_V e^{(E_V - E_C)/kT} = N_C N_V e^{-E_G/kT}. \tag{2.12}$$

$$n_i = \sqrt{N_C N_V} e^{(E_V - E_C)/2kT} = \sqrt{N_C N_V} e^{-E_G/2kT} \tag{2.13}$$

The Fermi energy in an intrinsic semiconductor, $E_i = E_F$, is given as[18]

$$E_i = \frac{E_V + E_C}{2} + \frac{kT}{2} ln\left(\frac{N_V}{N_C}\right) \tag{2.14}$$

which is located slightly midway of the bandgap in most cases.

By introducing specific impurities, the conductivity can be easily controlled. These impurities are called donors and acceptors. They essentially alter the hole and electron numbers in their respective bands and allows for the creation of n-type and p-type semiconductors when introduced in a controlled manner. In n-type semiconductors, electrons are the primary carriers of current. In p-type semiconductors, the primary carriers of current are holes. This is essentially the premise of how p-n junction solar cells are created. The number of the introduced ionized acceptors and donors can be estimated by[18]

$$N_A^- = \frac{N_a}{1 + g_A e^{(E_A - E_F)/kT}} = \frac{N_A}{1 + e^{(E'_A - E_F)/kT}}. \tag{2.15}$$

and

$$N_D^+ = \frac{N_D}{1 + g_D e^{(E_F - E_D)/kT}} = \frac{N_D}{1 + e^{(E_F - E'_D)/kT}} \tag{2.16}$$

Here, the site degeneracy factors for the acceptor and donor concentrations are g_A and g_D, respectively. The Fermi energy for the case where the acceptors and donors are assumed to be ionised, i.e $n_0 \simeq N_D$ and $p_0 \simeq N_A$ are given by[18]

$$E_F = E_i + kTln\left(\frac{N_D}{n_i}\right) \tag{2.17}$$

$$E_F = E_i - kTln\left(\frac{N_A}{n_i}\right) \tag{2.18}$$

for the n- and p-type materials, respectively. Here E_i is given by equation 2.14

Huge concentrations of added dopants create a major disturbance to the overall semiconductor system and a thorough study of how they affect the band structure must be also appraised. This axcess doping generally results in bandgap reduction, and thus causes the intrinsic carrier concentration to increase. This ultimately results affects the solar cell performance as will be studied in this work.

2.1.3 Light absorption

The process of creating electron-hole pairs through sunlight photon absorption underpins solar cell operation. Fundamental absorption is the process whereby an electron is excited directly from the valence band into the conduction band. A hole is left behind in the valence band in this process. The total energy of the process, together with the momentum of the constituent particles that partake in the absorption process should be conserved. Since the crystal momentum has large orders of magnitude compared to the photon momentum (i.e $p_\lambda = h/\lambda$ and $p_{crystal} = h/l$ where $l \ll \lambda$),the photon absorption process effectively conserves the electron's momentum[18].

The absorption coefficient that corresponds to a particular photon with energy, $h\nu$, is given by the approximation[30]

$$\alpha(h\nu) \propto \sum P_{12} g_V(E_1) g_C(E_2) \tag{2.19}$$

Here, P_{12} gives the overall probabilty of an electron transitioning from a state, E_1, to state E_2, with initial state electron density $g_V(E_1)$ and final state availabity $g_C(E_2)$. A summation over all possible transitions between states where $E_2 - E_1 = h\nu$ is then done to give the equation 2.5. Photon absorption results in the formation of an electron-hole pair, whereby an electron excited into the conduction band leaves a hole in the valence band[31].

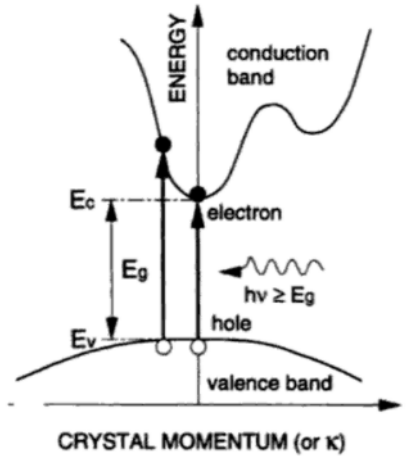


Figure 2.3: Photon absorption in a direct bandgap semiconductor (Sourced from [32])[33]

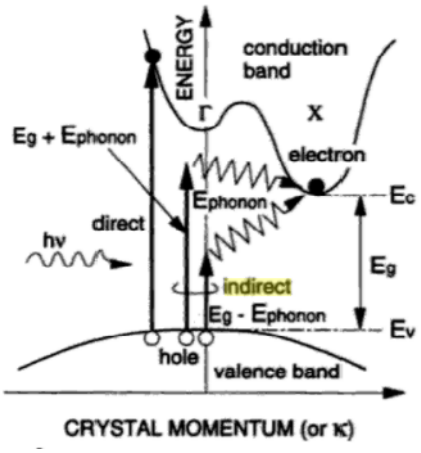


Figure 2.4: Photon absorption in an indirect bandgap semiconductor (Sourced from [32])

The basic photon absorption processes are shown in figure 2.3 and 2.4 for both direct and indirect bandgap semiconductors, respectively. In the case of direct bandgap semiconductors, both momentum and energy are conserved during the transition. From the energy conservation, the photon energy must be

$$h\nu = E_f - E_i, \tag{2.20}$$

For parabolic bands. We have that

$$E_V - E_i = \frac{p^2}{2m_p^*} \tag{2.21}$$

and similarly,

$$E_f - E_C = \frac{p^2}{2m_n^*} \tag{2.22}$$

From the equations 2.21 and 2.22, we obtain

$$h\nu - E_G = \frac{p^2}{2}\left(\frac{1}{m_n^*} + \frac{1}{m_p^*}\right) \tag{2.23}$$

.

The absorption coeffient for direct band gap transitions is approximately[30]

$$\alpha(h\nu) \approx C(h\nu - E_G)^{1/2}. \tag{2.24}$$

Here, C is a constant. Quantum selection rules don't allow for transitions at $p = 0$ for certain semiconductor materials, but permit only transitions for $p \neq 0$. In such cases we obtain[30]

$$\alpha(h\nu) \approx \frac{B}{h\nu}(h\nu - E_G)^{3/2}. \tag{2.25}$$

Here, D is a constant.
The valenceband maximum is found at a different crystal momentum from that of the conduction band minimum for indirect bandgap semiconductors[34]. This means that the process of absorption should involve another particle to ensure that the conservation of electron momentum is not violated. Phonons provide the additional energy since they possess a low energy and a high momentum. $\alpha(h\nu)$ for indirect bandgap transitions is slightly smaller than that of direct bandgap transitions. The absorption process for indirect bandgap transitions is illustrated in figure 2.4. The absorption coeffient in this type of process where a phonon is involved is given by(for the phonon absorption case)[30, 18]

$$\alpha_{abs}(h\nu) = \frac{B(h\nu - E_G + E_{ph})^2}{e^{E_{ph}/KT} - 1} \tag{2.26}$$

and for the phonon emission case,

$$\alpha_{emm}(h\nu) = \frac{B(h\nu - E_G - E_{ph})^2}{1 - e^{-E_{ph}/KT}} \tag{2.27}$$

In general the absorption coefficient for indirect band gap semiconductors is given by

$$\alpha(h\nu) = \alpha_{abs}(h\nu) + \alpha_{emm}(h\nu) \tag{2.28}$$

Figure 2.5 shows the relationship between the α and $h\nu$ for a direct bandgap and an indirect band gap material. Since α is relatively small for indirect transitions, light penetrates more in indirect bandgap semiconductors for energies around the bandgap energy of conventional solar cells. Figure 2.5 also shows that although the processes described are dominant, it is also

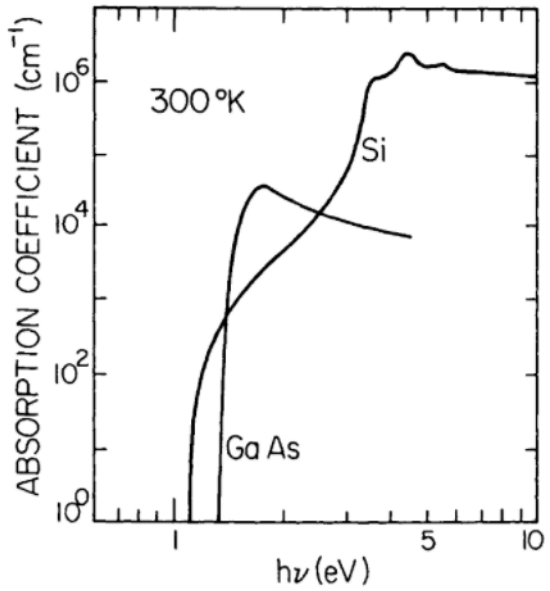


Figure 2.5: Absorption coefficient given as a function of photon energy for indirect(Si) and direct(GaAs) bandgap materials
(Sourced from [35])

possible to have a direct bandgap transition in an indirect bandgap semiconductor provided that the energy of the photon is large enough.

2.2 Carrier generation

The rate at which electron-hole pairs are formed in solar cells under illumination as a function of position is called the generation rate. It is expressed as the number of electron-hole pairs per unit volume per second)[34]. It is given as

$$G(z) = (1 - S_f) \int_{\lambda} (1 - r(\lambda))\phi(\lambda)\alpha(\lambda)e^{\alpha z} d\lambda. \tag{2.29}$$

Here, the grid shadowing factor is denoted by S_f, r(λ) denotes the reflectance from the surface, $\alpha(\lambda)$ gives the absorption coefficient expressed in terms of wavelength from the relationship $h\nu = hc/\lambda$. $\phi(\lambda)$ is the incident photon flux. One can assume that sunlight is incident at $z = 0$. The incident flux is computed by taking the incident spectral power density at each corresponding λ and dividing it by the photon energy[18]. The generation rate is essentially a function of $\alpha(\lambda)$ and $\phi(\lambda)$.

2.3 Recombination

When semiconductor devices are driven from thermal equilibrium by current injection or an illumination source, the electron and hole concentrations tend to go back to their equilibrium states. This is done by an electron decaying from the conduction band to combine with a valence band hole in a process that is reffered to as recombination. The three recombination mechanisms that are discussed here are recombination through defects(traps) within the bandgap, Auger recombination and band-to-band(radiative) recombination. These recombination processes are shown in figure 2.6.

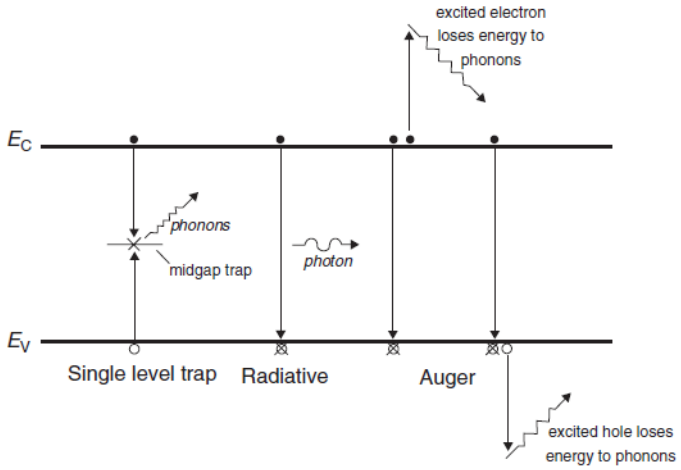


Figure 2.6: Recombination processes in solar cells
(Sourced from [35])

The overall recombination rate in the semiconductor device per unit volume per second through a single level trap (SLT) situated at an energy E_T in the bandgap is described by[36]

$$R_{SLT} = \frac{pn - n_i^2}{\tau_{SLT,n}(p + n_i e^{(E_i - E_T)/kT}) + \tau_{SLT,n}(n + n_i e^{(E_T - E_i)/kT})}. \tag{2.30}$$

In equation 2.30, the carrier lifetimes are expressed as[36]

$$\tau_{SLT,i} = \frac{1}{\sigma_i \nu_{th} N_T}. \tag{2.31}$$

In the above equations, the capture cross sections σ_i for holes and electrons are denoted by σ_p and σ_n, respectively. The thermal velocity is denoted

by ν_{th} for the carriers and N_T denotes the trap concentration.

The above equation can be simplified by making a few assumptions. If the material has a carrier injection ($n_0 \leq n \ll p_0$) and is p-type ($p \approx p_0 \gg n_0$) and $E_T \approx E_i$, then the R_{SLT} is simplified to[18]

$$R_{SLT} \approx \frac{n - n_0}{\tau_{SLT,n}}. \tag{2.32}$$

The minority carriers essentially dominate the rate of recombination because there are a lot more majority carriers than minority carriers.

In conditions of high injection ($p \approx n \gg n_0, p_0$),

$$R_{SLT} \approx \frac{n}{\tau_{SLT,p} + \tau_{SLT,n}} \approx \frac{p}{\tau_{SLT,n} + \tau_{SLT,p}}. \tag{2.33}$$

Radiative recombination

Radiative recombination is the optical generation process in reverse and is more prevalent in semiconductors with direct bandgaps. In this process, the decaying electron's energy is passed on to an emmited photon. This is the basic operation of semiconductor lasers and LED's. The net recombination rate arising from the radiative process is[37][18]

$$R_\lambda = D(pn - n_i^*). \tag{2.34}$$

Here, D is just a constant and n_i^* is the intrinsic carrier concentration as explained. For a low-injected n-type semiconductor, R_λ can be expressed in terms of an effective lifetime τ_λ. This is given by[18]

$$R_\lambda \approx \frac{p - p_0}{\tau_\lambda}. \tag{2.35}$$

The effective lifetime τ_λ is given by[18]

$$\tau_\lambda = \frac{1}{n_0 B} \tag{2.36}$$

For p-type semiconductors where high injection prevails,

$$R_\lambda \approx Bp^2 \approx Bn^2 \tag{2.37}$$

the photons released during the recombination process can be reabsorbed if the solar cell is well designed through a process called photon recycling[38].

Auger recombination

Auger recombination is a recombination process where the transition energy is passed onto another carrier in either the valence or conduction band, which then relaxes thermally as is illustrated in figure 2.6. The resulting recombination rate due to the Auger-process is[18]

$$R_{Auger} = (C_n n + C_p p)\,(pn - n_i^*)\,. \tag{2.38}$$

In a low-injected n-type material, the net auger recombination rate is given by[18]

$$R_{Auger} \approx \frac{p - p_0}{\tau_{Auger,p}} \tag{2.39}$$

where

$$\tau_{Auger,p} = \frac{1}{C_n n_0^*}. \tag{2.40}$$

In high-injection conditions in the p-type material($p \approx n \gg p_0, n_0$), we have

$$R_{Auger} \approx (C_n + C_p)\,p^3 \approx (C_n + C_p)\,n^3 \tag{2.41}$$

All the recombination processes occur in parellel. Thus, the net recombination rate is the summation of all the rates from each process[18]. This results in the recombination term that is given by[18]

$$R = \left[\sum_{traps,i} R_{SLT,i}\right] + R_\lambda + R_{Auger} \tag{2.42}$$

The overall effective minority-carrier lifetime (τ^{-1}) for a low-injection doped semiconductor is

$$\frac{1}{\tau} = \left[\sum_{traps,i} \frac{1}{\tau_{SLT,i}}\right] + \frac{1}{\tau_\lambda} + \frac{1}{\tau_{Auger}}. \tag{2.43}$$

Usually, interfaces between two material types have a large concentration of defects as a result of a sudden termination of the crystal lattice. This gives rise to a region of a non-ending traps within the badgaps at the surface called surface states. These surface states are given by R_S(rate per unit area per second)[36]

$$R_S = \int_{E_V}^{E_C} \frac{pn - n_i^2}{(p + n_i e^{(E_i - E_t)/kT})/s_n(E_t) + (n + n_i e^{(E_t - E_i)/kT})/s_p(E_t)} D_{\prod}(E_t) d(E_t). \tag{2.44}$$

Here, the trap energy is given by E_t. $D_{\prod}(E_t)$ denotes the surface state, and the surface recombination velocities are expresses as $s_n(E_t)$ and $s_p(E_t)$. The surface recombination velocities can be thought of as carrier lifetimes for bulk traps. For the purpose of modeling the devices, the Surface recombination rate can be simplified to be[36]

$$R_S = S_p(p - p_0), \tag{2.45}$$

$$R_S = S_n(n - n_0). \tag{2.46}$$

for the n- and the p-type materials.

S_p and S_n are the effective recombination velocities which are often treated as constants independent of carrier concentration, which is often is not really the case.

2.4 Carrier transport

The behaviour of holes and electrons is like that of free particles of the same electronic charge. These charged particles are described by their effective masses m_p^* and m_n^*, respectively. They also undergo the diffusion and drift processes. Drift is described by charged particle motion due to an applied electric field. With no disturbance, electrons and holes will continue to accelerate through the semiconductor without limits. This never happens in reality since the carriers interact crystal atoms, dopant atoms, defects, etc. The carriers will follow a general direction dictated by the applied electric field, $\vec{E} = -\nabla\phi$.The electrostatic potential ϕ also accounts for the band parameters that represent the effects of degeneracy and electron affinity[39]. Therefore the carriers seem as though they are moving at a constant drift velocity, $\vec{v}_d$ which is directly proportional to the electric field and is given as[18]

$$|\vec{v}_d| = \left|\mu\vec{E}\right| = |\mu\nabla\phi| \,. \tag{2.47}$$

Here, μ denotes the carrier mobility which is independent of the electric field strength unless the field is very strong, which is typically not the case in solar cells[18]. The drift current densities for the electrons and holes is given as[18]

$$\vec{J}_n^{drift} = qn\vec{v}_{d,n} = q\mu_n n\vec{E} = -q\mu_n n\nabla\phi \tag{2.48}$$

and

$$\vec{J}_p^{drift} = qp\vec{v}_{d,p} = q\mu_p p\vec{E} = -q\mu_p p\nabla\phi. \tag{2.49}$$

Lattice (phonon) and impurity scattering are the most important scattering mechanisms. In the device modeling of solar cells, one can use carrier mobilities in Si at 300 K which are very well approximated by[40]

$$\mu_n = 92 + \frac{1268}{1 + \left(\frac{N_D^+ + N_A^-}{1.3\times10^{17}}\right)^{0.91}} cm.V^{-1}.s^{-1} \tag{2.50}$$

$$\mu_p = 54.3 + \frac{406.9}{1 + \left(\frac{N_D^+ + N_A^-}{1.3\times10^{17}}\right)^{0.88}} cm.V^{-1}.s^{-1} \tag{2.51}$$

These two carrier mobilites are plotted in figure 2.7.

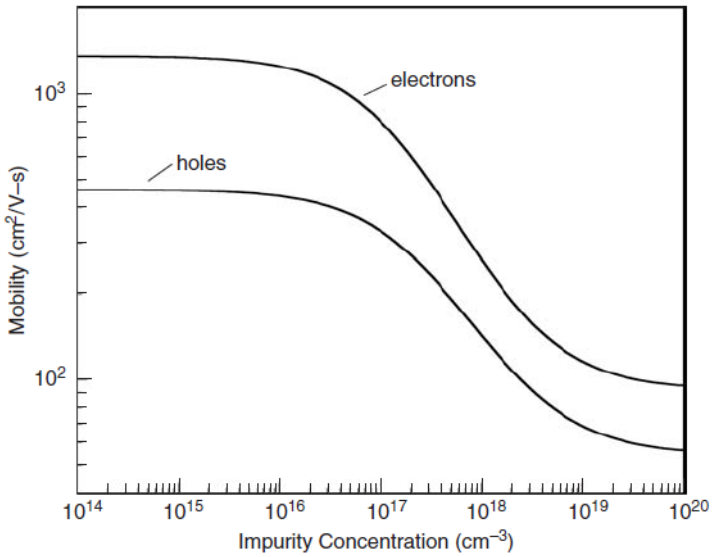


Figure 2.7: Mobilites for silicon at 300 K
(Sourced from [18])

At high levels of impurity concentration, the mobility is controlled by ionized impurity scattering, and at low levels intrinsic lattice scattering prevails.

Electrons and holes will tend to distribute themselves evenly within the semiconductor when there are no external forces. This phenomenon is called diffusion. The diffusion current densities for holes and electrons, respectively, are given by[18]

$$\vec{J}_p^{diff} = -qD_p\nabla p \tag{2.52}$$

$$\vec{J}_n^{diff} = qD_n\nabla n \tag{2.53}$$

Here, D_n and D_p are the electron and hole diffusion coefficients, respectively. There cannot be any net electron or hole current in thermal equilibrium. This results in the Einstein relationship which permits for the diffusion coefficient to be determined from the knowledge of the mobility. For nondegenerate materials it is given by[18]

$$\frac{D}{\mu} = \frac{kT}{q} \tag{2.54}$$

The total electron and hole current densities from the current contributions from the drift and diffusion components[18] are

$$\vec{J_p} = \vec{J_p^{drift}} + \vec{J_p^{diff}} = q\mu_p p\vec{E} - qD_p\nabla p = -q\mu_p p\nabla\phi - qD_p\nabla p \qquad (2.55)$$

,and

$$\vec{J_n} = \vec{J_n^{drift}} + \vec{J_n^{diff}} = q\mu_n n\vec{E} - qD_n\nabla n = -q\mu_n n\nabla\phi - qD_n\nabla n \qquad (2.56)$$

Which gives the total current as

$$\vec{J} = \vec{J_p} + \vec{J_n}. \qquad (2.57)$$

2.5 Semiconductor device equations

The semiconductor device equations which were initially described by Van Roosbroeck[41] are used to explain solar cell operation. These equations are the Poisson's equation and the 2 continuity equations for holes and electrons, respectively. The Poisson's equation is given by[18]

$$\nabla.\varepsilon\vec{E} = q\left(N + p - n\right). \tag{2.58}$$

Here, N is the net charge that arises because of the dopants and other trapped charges (N=N_D-N_A), and n and p are the electron and hole carrier concentrations as explained. The electron and hole continuity equation are given by[18]

$$\nabla.\vec{J_n} = q\left(R_n - G + \frac{dn}{dt}\right) \tag{2.59}$$

$$\nabla.\vec{J_p} = q\left(G - R_p - \frac{dp}{dt}\right). \tag{2.60}$$

Here, G is the rate of carrier generation and $R_{p,n}$ is the recombination rate for the carriers. The semiconductor equations are solved at numerically using a set of boundary conditions. The primary variables are the equilibrium carrier concentrations, Fermi level (quasi-Fermi-levels for systems driven out of thermodynamic equilibrium by a voltage bias, a light bias or both), charge mobilities, bandgap and the permittivity.

2.6 Minority-carrier diffusion equation

In uniformly doped semiconductors, carrier mobilities, diffusion coefficients, electric permittivity and bandgap are independent of position. This means that in steady state solar cell operation ($\frac{dn}{dt} = \frac{dp}{dt} = 0$), the semiconductor equations become (for ∇ in the x-direction)[18]

$$\frac{d\vec{E}}{dx} = \frac{q}{\epsilon}\left(p - n + N_D - N_A\right) \tag{2.61}$$

$$q\mu_n \frac{d}{dx}\left(n\vec{E}\right) + qD_n \frac{d^2n}{dx^2} = q\left(R - G\right) \tag{2.62}$$

$$q\mu_p \frac{d}{dx}\left(p\vec{E}\right) - qD_p \frac{d^2p}{dx^2} = q\left(R - G\right) \tag{2.63}$$

In quasi-neutral regions, which are regions a good distance away from the p-n junction, the electric field becomes insignificant. The drift current becomes insignificant and can effectively be ignored when compared to the diffusion current when one considers low level injection and the minority carrier. This means that the recombination term R reduces to[18]

$$R = \frac{n_P - n_{P_0}}{\tau_n} = \frac{\triangle n_P}{\tau_n} \tag{2.64}$$

$$R = \frac{p_N - p_{N_0}}{\tau_p} = \frac{\triangle p_N}{\tau_p} \tag{2.65}$$

in the p- and the n-type regions, respectively. These $\triangle p_N$ and $\triangle n_P$ are the excess minority-carrier concentrations [42]. The capitalized subscripts in equation 2.64 and 2.65 describe quantities in the n- and p-type regions. The lower case subscripts are used to indicate quantities associated with minority carriers in each region. Therefore, the equations above reduce to what are called the minority-carrier diffusion equations. These equations are given by

$$D_p \frac{d^2 \triangle p_N}{dx^2} - \frac{\triangle p_N}{\tau_p} = -G(x) \tag{2.66}$$

$$D_n \frac{d^2 \triangle n_P}{dx^2} - \frac{\triangle n_P}{\tau_n} = -G(x) \tag{2.67}$$

for the n- and the p-type materials, respectively.

2.7 Summary

The important physical properties and parameters that define the functioning of solar cell devices have been explored. The next chapter will look at the different figures of merits that characterise a solar cell.

Chapter 3

Solar cell operation and performance

In this chapter, the various figures of merit used to estimate solar cell performance are discussed. These properties are arguably the most essential tools used for solar cell comparison and selection of materials and device concepts for photovoltaic applications.

3.0.1 Solar cell parameters

An ideal solar cell can simply be represented by a current source that is connected in parallel with a rectifying diode to account for the recombination effects in the quasi-neutral regions and the depletion region[18]. The I-V characteristic of such a cell is described by the shockley solar cell equation[43] given by

$$I = I_{ph} - I_o \left(e^{qV/kT} - 1 \right). \tag{3.1}$$

Here, k is the Boltzmann constant, q the electron charge, V the voltage at the cell terminals and T is the absolute temperature. The Shockley equation serves as a reminder that a solar cell in the dark is simply a diode. The photo generated current I_{ph} is related to the photon flux of the incident sunlight. I_0 is the diode saturation current. The figures of merit which are important in analysing device performance are the short-circuit current(I_{SC}), the open-circuit voltage(V_{OC}), and the fill factor(FF). I_{SC} is the current obtained when the voltage across the solar cell is 0. This is the highest current that can be obtained from a given solar cell. At open-circuit (I=0) all the light-generated current flows through the diode and the open-circuit voltage is given by[44]

$$V_{OC} = \frac{kT}{q} ln \left(\frac{I_{SC} + I_o}{I_o} \right). \tag{3.2}$$

This is the maximum voltage attainable from the solar cell. The most important point on the I-V curve is the point where the maximum power is obtained. This is the maximum power point where $V = V_M$ and $I = I_M$. This point produces a rectangle with the largest area under the curve. The maximum power is given by $P_{max} = V_M I_M$. It is convenient to compute FF which is the ratio of the maximum power P_{max} and the product of I_{SC} and V_{OC}. FF gives an indication of the "squareness" of the solar cell I-V characteristic, and it is less than 1. It is given by[45]

$$FF = \frac{V_M I_M}{V_{OC} I_{SC}} = \frac{P_{max}}{V_{oc} I_{SC}} \tag{3.3}$$

The power conversion efficiency, η, is plausibly the most crucial figure of merit for the comparison of different solar cells. It is used to compare the performance of one solar cell to another. It is defined as the ratio of the maximum power output from the solar cell to the input power from the sun. The efficiency is dependent on the cell's temperature, and the spectral intensity of the incident light. The power conversion efficiency is defined by[15]

$$\eta = \frac{P_{MP}}{P_{in}} = \frac{FF V_{OC} I_{SC}}{P_{in}}. \tag{3.4}$$

3.1 Summary

The figures of merit that define solar cell performance have been explained. The next chapter looks at the different simulation programs that make use of the physical properties and principles discussed in chapter 2, together with the performance parameters discussed in chapter 3.

Chapter 4

Simulation software

This chapter serves as an introduction to different simulation software programs. Although all the software programs solve the semiconductor equations with appropriate boundary conditions, there might exist some pros or cons which might persuade the reader to choose one software over the other. Sample simulations are done for each software package discussed using the key input parameters required. This is not an exhaustive list of all the available software packages, but rather gives an opportunity for the reader to familiarise themselves with some of the most common programs which are free to download and may be used within the confines of the user license.

4.1 AMPS1D

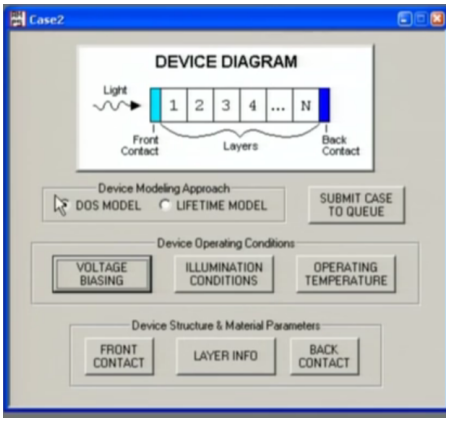


Figure 4.1: Main Screenshot for AMPS1D

AMPS is a general and user friendly simulation program that was devel-

oped by Prof Stephen Fonash and his post-doctoral students at the Pennsylvania State University. AMPS stands for Analysis of Microelectronic and Photonic Structures[16]. It is an easy-to-use tool for the study of semiconductor devices and solar cell device designs[46]. The software allows for 1-Dimensional analysis of two terminal devices such as diodes, sensors, photodiodes and photovoltiac devices. AMPS has been a very effective tool in aiding the understanding of device operation and device physics for single crystal, amorphous and poly-crystalline device structures. AMPS-1D has made significant breakthroughs in the explanation of the red kink and the transient effect in poly-crystalline solar cells such as CdS/CIGS solar cell devices[47]. The software was utilized to show that thin film silicon structures, which exibit light trapping, have the capability of delivering competitive solar cell power conversion efficiencies.It has also been used to determine the optimum structure of a solar cell, light and voltage biasing conditions[47]. It boasts an easy to use interface,as illustrated in figure 4.1, and a user can work on more than one problem at a time. Each device simulated can have layers up to a total number of 30, with each layer having different material parameters. The setup of a simulation is simple, and the help function is comprehensive and well supported by a user manual. Absorption coefficients must be manually entered as a function of wavelength on a grid, which could be an easy task if the data could be taken from an external file. The results obtained are saved on an external file, however, the inability to save the images of the graphs in the well-known formats such as JPEG and PNG can be quite inconvenient.

Figure 4.2 shows a simple silicon based P-N junction device simulation output using the AMPS software package. The main input parameters are the permittivity, electron affinity, electron and hole effective densities, electron and hole mobilities and the doping concentrations. Standard AM1.5 spectrum is used for the simulation.

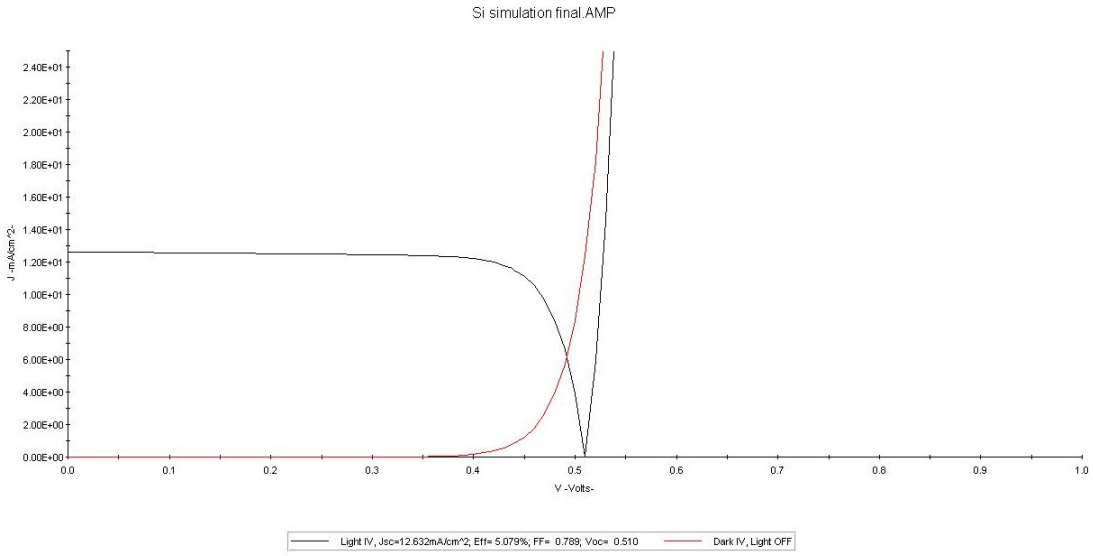


Figure 4.2: Sample Si simulation using AMPS1D

4.2 WxAMPS

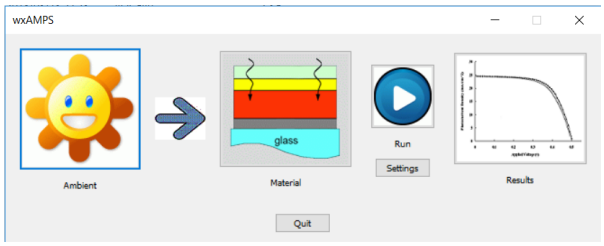


Figure 4.3: Main Screenshot for WxAMPS

WxAMPS serves as an upgrade for the solar cell simulation program AMPS1D (Analysis of Microelectronic and Photonic Structures) that was originally written by Fonash et al. The user interface of wxAMPS is more user friendly as can be seen in figure 4.3, and more aesthetically pleasing for parameter entries and results outputs. It also provides a cross-platform library and quick data entry for input variables that the user needs to analyse for different solar devices. Ambient, material and the results tab allows for easy navigation and input of these variables for different materials and solar cell devices. Each device layer can be configured independently with easy access for the material's optical and electrical properties as shown in figure 4.4, which is beneficial when working with multi-junction solar cells. Standard data for the ambient parameter conditions such as the widely used

AM1.5 spectrum come standard with the program installation, together with standard material absorption properties for well understood materials such as silicon. Beyond what the original AMPS kernel provided, wxAMPS also includes tunneling models and has a sophisticated algorithm that combines the Gummel and Newton methods[48]. The inclusion of a trap-assisted tunneling model in the upgraded program results in more precision of the Tandem cells simulations. The combination of the Gummel and Newton method solutions improve the code stability and allow the tunneling models to function well within the algorithm. Since there is an option for adding an unlimited number of layers, modeling graded solar cells is easily implemented in wxAMPS[48].

Figure 4.5 shows a simple silicon based P-N junction device simulation output using the wxAMPS software package. The main imports are the permittivity, electron affinity, hole and electron effective densities, electron and hole mobilities and the doping concentrations. Standard AM1.5 spectrum is used for the simulation as before.

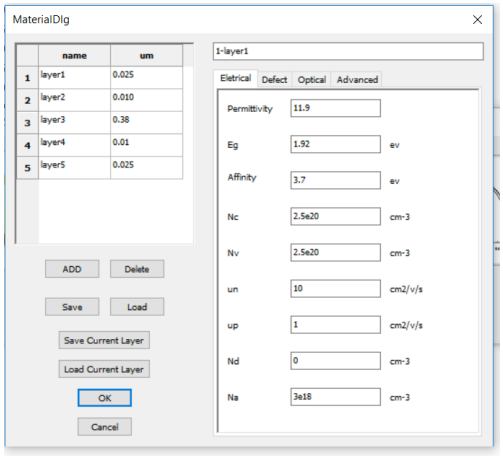


Figure 4.4: Material parameters screenshot for WxAMPS

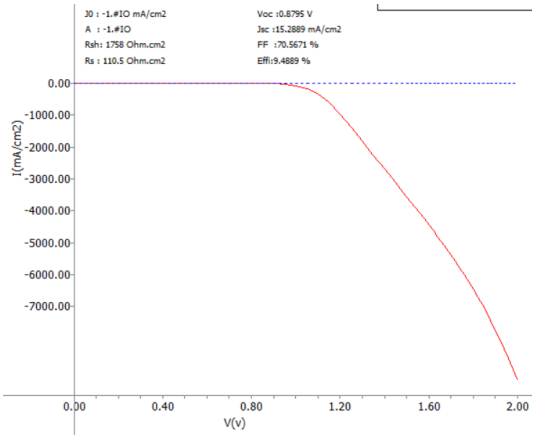


Figure 4.5: Sample simulation using WxAMPS

4.3 PC1D

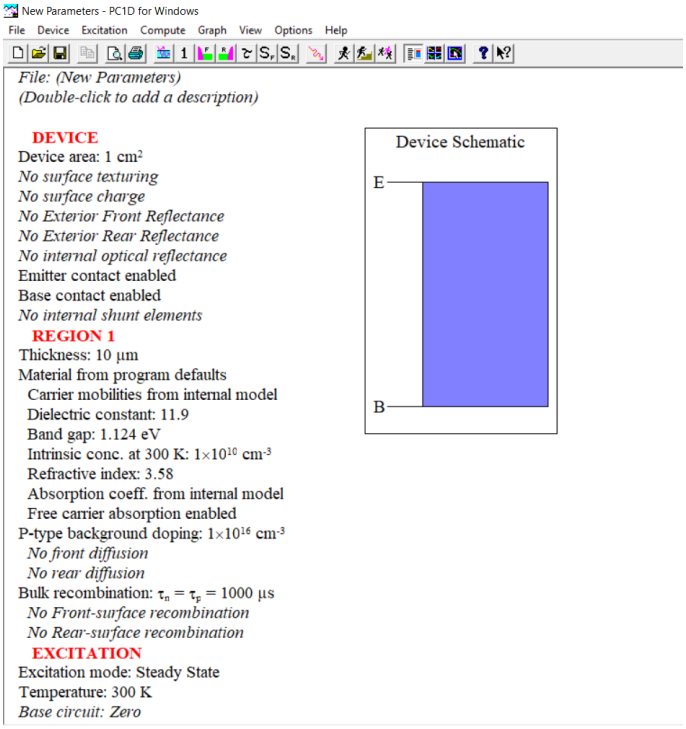


Figure 4.6: Main screenshot for PC1D

This simulation programme was written at Sandia national labs by Basore and coworkers, and advancement of the software was undertaken at Univer-

sity of New South Wales (UNSW), Australia[49]. It has been considered by the PV research community as one of the baseline programs for silicon solar cell modeling. It has a user-friendly interface and makes it easy for users to define a new device problem, as shown in figure 4.6. Values of parameters for each layer added in the device can be altered by a single click on the relevant parameter concerned from the parameter list on screen for that layer, or parameters can be changed through the menu system available on the program. This makes it relatively easy for user to see the effect of different parameters on the performance of the overall device. The option for the number of layers added is only 5 in this software[46]. However, this is sufficient for devices such as CdTe or CdS in cases where the layer doping is not graded.Common recombination mechanisms are well implemented within the program. The space charge that is connected to these levels is 0 because no densities of the associated deep levels can be given. This shortfall makes the program unsuitable for use when modeling amorphous silicon cells, since the space charge contained by deep states is quite essential in this use. Apart from the conventional J(V) characteristics and spectral response simulations, light or bias voltage can be abruptly applied and their effects can be studied with respect to time. The simulation results can be copied to external programs.

Figure 4.7 shows a simple silicon based P-N junction device simulation output using the PC1D software package. The main imports are the permittivity, electron affinity, effective densities, carrier mobilities and the doping concentrations. Standard AM1.5 spectrum is used for the simulation.

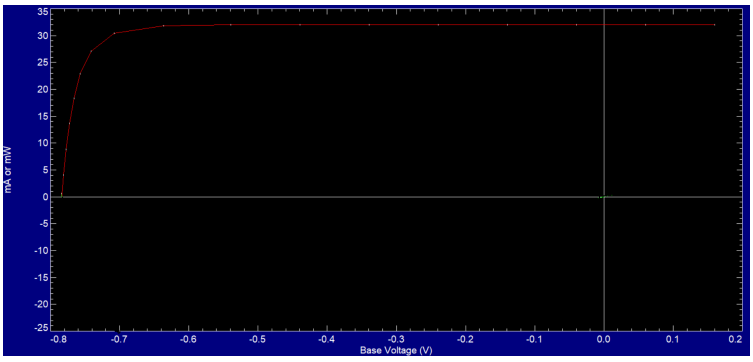


Figure 4.7: Sample simulation using PC1D

4.4 SCAPS

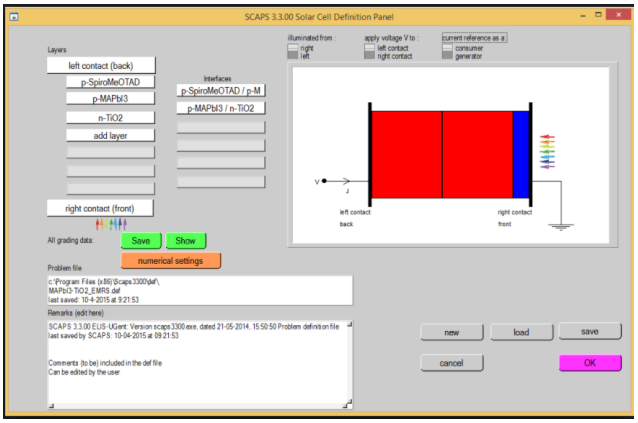


Figure 4.8: Main screenshot for SCAPS

SCAPS is a numerical simulation program that is designed to simulate polycrystalline thin-film devices. It's used for simulating CIGS/CIS and CdTe-based solar cells[50]. The user interface is pretty much straightforward and entering a new problem is relatively easy. All physical and electronic properties for each layer added can be easily altered on a separate window. THe basic models for the dependence of parameters such as the effective density of states and the ν_{th}, on temperature are used, and other parameters such as μ and bandgap are modeled as being temperature dependent. Due to the limitation of only 7 layers, the programs suitability for graded junctions is not ideal. Recombination that occurs within the bulk levels and the occupation of these states is described by the SRH formalism, and recombination at the interface states is governed by a broader version of the SRH formalism. The extension allows electron exchange between the interface state and the two adjacent conduction bands, and of holes between the interface state and the two adjacent valence bands[46]. SCAPS can produce simulations using the greatest number of electrical measurements and each measurement can be computed for both dark and light conditions as a function of temperature. The outputs for the simulation can be easily saved to an output file, making it easy for result comparison with other programs.

Figure 4.9 shows a simple silicon based P-N junction device simulation output using the SCAPS software program. The input parameters are the permittivity, electron affinity, effective densities, carrier mobilities and the doping concentrations. Standard AM1.5 spectrum is used for the simulation.

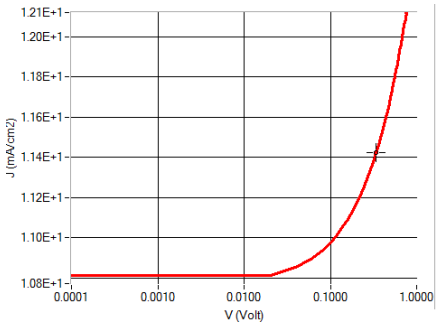


Figure 4.9: Sample simulation using SCAPS

4.5 GPVDM

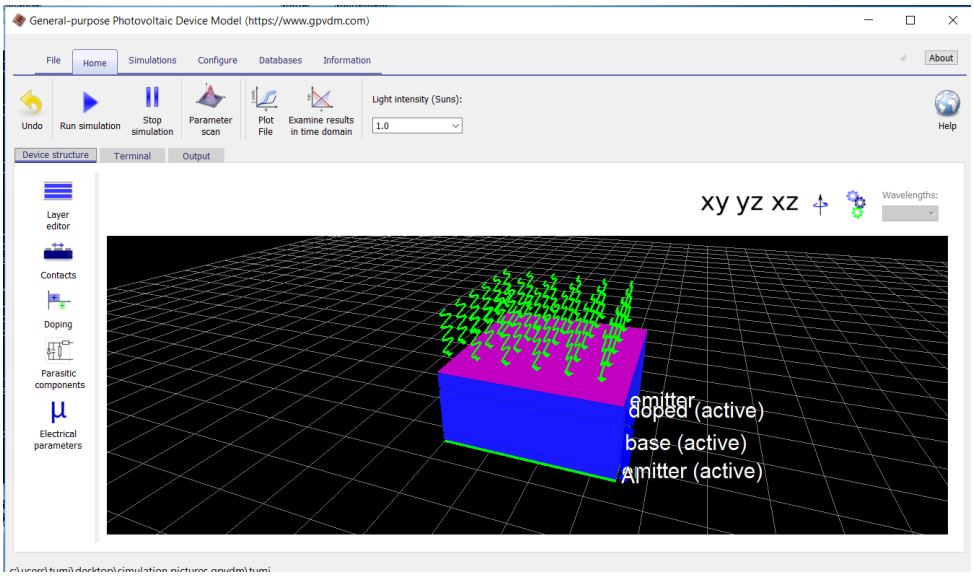


Figure 4.10: Main screenshot for GPVDM

GPVDM is a free simulation tool that is used in the simulation of opto-electronic devices. It was developed by Roderick Mackenzie, who is a professor at the University of Nottingham [51]. It can simulate devices such as OPV's, OLEDS, OFETS, organic solar cells, c-Si solar cells, a-Si solar cells and CIGS solar cells. The model that is used in the program to produce the simulations makes use of a finite difference approach to solve both the hole and electron drift-diffusion equations in position space, and to describe the charge movement inside the solar cell device. It boasts an easy to use interface thats illustrated in figure 4.10 and the program is available for use with

most operating systems such as windows and linux. The device parameters are easily accessible through an easy to navigate user interface. The model solves the device equations in steady state in 1D or 2D. It uses the SRH formalism to handle recombination and carrier trapping[52].

Figure 4.11 shows a simple silicon based P-N junction device simulation output using the GPVDM software program. The main imports are the permittivity, electron affinity, effective densities, carrier mobilities and the doping concentrations. Standard AM1.5 spectrum is used for the simulation.

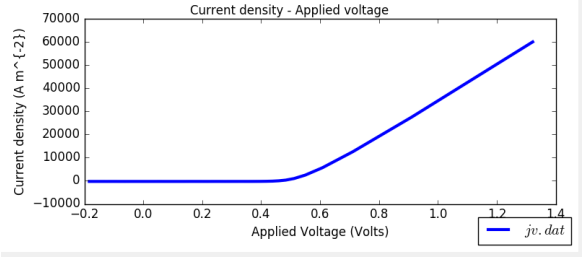


Figure 4.11: Sample simulation using GPVDM

4.6 Chapter summary

This chapter has served to discuss some of the available device simulation programs for solar cell devices. The software packages discussed here are not an exhaustive list but rather introduced some of the most popular device simulation packages. WxAMPS is the programme that shall be used for the generation of the more advanced results in chapter 5 and 6. WXAMPS offers an easy-to-use interface and it is very easy to install and to operate. It is also free to download, which makes it an ideal choice for academic research like the simulations that will be generated in the later chapters.

Chapter 5

Device simulations

This chapter explains how to model a simple solar cell device using the WxAMPS device simulation program. We will see how device material properties and overall structure work together in determining the resultant performance of our device under a given temperature, model irradiation and applied voltage.

Ambient settings

After running the WxAMPS program, the 3 tab options given are the ambient, material and results tab as shown in figure 4.3. The ambient tab allows the user to set all the parameters that are not material dependent and it can be kept constant for the devices that are being modelled. It is always wise to keep these ambient parameters constant when comparing the performance of two or more solar cell devices. Under the ambient tab, the temperature at which the device will be operating is can be set. Light conditions such as AM1.5 or AM1.5G are also set under this tab, where an external file is loaded containing the desired spectra. The program, like most device simulalation programs, comes with standard spectra that can be used. The QE option allows for the selection of the range of wavelengths which the quantum efficiency can be calculated.

Next, one has to select the desired contact parameters. "PHI(eV)" allows one to input the barrier heights of the contacts. "Sn0" and "Sp0" denote the surface recombination velocities for the minority and the majority carriers in both the top and the bottom contacts. "RF" is the reflection coefficient which is a parameter that essentially describes the proportion of the incoming photons being reflected off the top and bottom contact. Its values range from 0 for no reflection to 1 for total reflection. Total reflection means that

all of the incoming light is reflected off the surface and zero reflection means no light is reflected off the surface. The bias voltage option allows one to specify the range of voltages in which the semiconductor equations should be solved. This is advantageous, because it allows the user to set large voltage steps near the short circuit voltage and smaller voltage steps closer to the open circuit voltage, which is viable for the overall reduction in computation time.

Table 5.1 shows the set of ambient parameters to be used for the simulations. These parameters will be kept fixed for the simulations that will be done in this chapter.

Table 5.1: Ambient properties for simulations

Parameter	**Value**
Temperature	300 K
Spectrum	AM1.5 full
Barrier height (top)	0
Barrier height (bottom)	0
Surface recombination velocities (all)	1×10^{7}
Reflection coeffient (top)	0
Reflection coefficient (bottom)	1

Material properties

The material properties tab allows the user to design the solar cell device and to modify the characteristics of each layer. The user has the option to add layers, delete an unwanted layer, load a layer from the layer database in the external files, and save the solar cell configured for analysis at a later stage. Each of the layers are configured independently and the user can choose to modify the parameters as desired. For each layer, the user can modify the electronic, defect, optical and other material properties by navigating through the tabs for each set of properties. The electronic properties include the permittivity, bandgap, electron affinity, electron and hole effective densities, charge carrier mobilities and the doping concentrations for both the electrons and holes. The electronic properties, except for the permittivity, electron affinity and doping concentrations can be either found in the litera-

ture, or be calculated by using ab initio methods as done in [53].

In the computation of ab initio calculated parameters, an understanding of the underlying numerical methods that the physical models are based on is essential to obtaining reliable results. The useful properties that can be used as data imported to the solar cell device simulations are the effective masses for the electrons and the holes, the charge carrier mobilities, the band gap, and the absorption coefficients. A brief explanation of how these parameters are obtained is given below, with reference to bulk silicon parameters. The experimental lattice constant used is 5.431 nm[54].

The electronic ground state of the many electron system is computed using the quantum esspresso package[55] which makes use of density functional theory (DFT) based methods. The Perdew-Becke-Ernzerhof (PBE) functional[56] is used in this case to describe the exchange-correlation potential, since it offers a high degree of transferability. More accurate functionals can be employed in special situations. A suitable norm-conserving pseudopotential such as the Goedecker-Hartwigsen-Hutter-Teter norm-conserving pseudo-potentials[57] was used for the description of the core electrons.
The DFT computed band structure of silicon is given in figure 5.1.

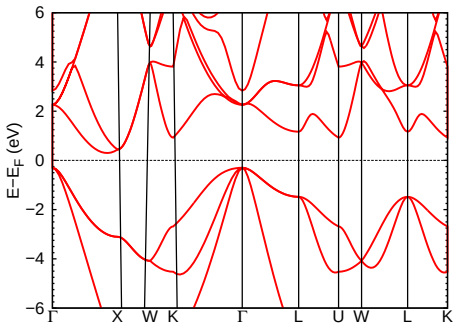


Figure 5.1: DFT-PBE band structure of Si.
(Courtesy of Khaled)

Although the bandgap is underestimated by DFT methods, the form of the curvature of the bands is quite reliable for the calculation of the effective masses. The effective masses of the charge carriers are calculated from the curvature of the conduction and valence band minimum and maximum, respectively. More specifically, the effective masses of a band n at point $\mathbf{k}_0$ in

directions i, j are given by [58]

$$m_{ij}^{*} = \frac{\hbar^2}{2}\left[\frac{\partial^2 E_n}{\partial \mathbf{k}_i \partial \mathbf{k}_j}\right]^{-1}_{\mathbf{k}=\mathbf{k}_0}. \tag{5.1}$$

The carrier mobilities were calculated from the relaxation time using

$$\mu = \frac{e}{m^*}\tau_{\text{relax}}. \tag{5.2}$$

The relaxation time τ_{relax} is identical to the imaginary part of the electron self-energy at the center of the Brillouin zone. The relaxation time is obtained by computing the electron self-energy equation associated with the electron-phonon interaction which is given by [59, 60]:

$$\Sigma_{n\mathbf{k}} = 2\sum_{\mathbf{q}v} w_{\mathbf{q}} \left|g^{v}_{mn}(\mathbf{k},\mathbf{q})\right|^2 \left[\frac{n_{\mathbf{q}v} + f_{\epsilon_{m\mathbf{k}+\mathbf{q}}}}{\epsilon_{n\mathbf{k}} - \epsilon_{m\mathbf{k}+\mathbf{q}} + \omega_{\mathbf{q}v} - i\eta} + \frac{n_{\mathbf{q}v} + 1 - f_{\epsilon_{m\mathbf{k}+\mathbf{q}}}}{\epsilon_{n\mathbf{k}} - \epsilon_{m\mathbf{k}+\mathbf{q}} - \omega_{\mathbf{q}v} + i\eta}\right], \tag{5.3}$$

where $g^{v}_{mn}(\mathbf{k},\mathbf{q})$ are the electron phonon matrix elements given by

$$g^{v}_{mn}(\mathbf{k},\mathbf{q}) = \langle \psi_{m\mathbf{k}+\mathbf{q}} | \partial_{\mathbf{q}v} V | \psi_{n\mathbf{k}+\mathbf{q}} \rangle. \tag{5.4}$$

In Eq. (5.3) and Eq. (5.4) $\psi_{n\mathbf{k}}$ are the DFT wave functions of the nth band with wave vector $\mathbf{k}$, which have the corresponding band energies $\epsilon_{n\mathbf{k}}$ and Fermi occupations $f_{n\mathbf{k}}$. The frequency of the vth phonon branch at wave vector $\mathbf{q}$ is denoted by $\omega_{\mathbf{q}v}$, $n_{\mathbf{q}v}$ is its Bose occupation number. Furthermore, $\partial_{\mathbf{q}v}V$ is the derivative of the self-consistent potential associated with the vth phonon at $\mathbf{q}$. The numerical parameter $w_{\mathbf{q}}$ is the weight of the the point $\mathbf{q}$ in the Brillouin zone summation. The electron phonon matrix elements and the phonon wave functions were determined by Density Functional Perturbation Theory (DFPT) [61] as described in Ref. [62, 63].

The absorption coefficients were calculated from the knowledge of the dielectric $\varepsilon_M(\omega)$ constant using

$$\alpha(\omega) = \frac{2\omega}{c}\Im(\sqrt{\varepsilon_M(\omega)}). \tag{5.5}$$

In order to include excitonic effects the dielectric function can be computed using Bethe-Salpeter (BSE) in equation 5.6 and applying the standard Tamm-Dancoff Approximation [64, 65],where the (complex) macroscopic dielectric function is given by

$$\varepsilon_M(\omega) = 1 - \lim_{q\Rightarrow 0} v_{G=0}(q) \sum_{\lambda} \frac{|\sum_{n_1 n_2} \langle n_1 | e^{-iq\cdot r} | n_2 \rangle A^{(n_1 n_2)}_{\lambda}|^2}{\omega - E_\lambda + i\eta}. \tag{5.6}$$

with the BSE eigenstates λ, eigenvalues E_λ and coefficients $A_\lambda^{(n_1 n_2)}$ of the particle-hole pairs that contribute to this mode. The states n refer to whatever basis is used to expand the BSE states in, usually these are DFT states. Furthermore, $v_{G=0}(q)$ is the Coulomb kernel and η is a suitably chosen broadening parameter.

Figure 5.2 shows the results of the calculated absorption coefficients for silicon.

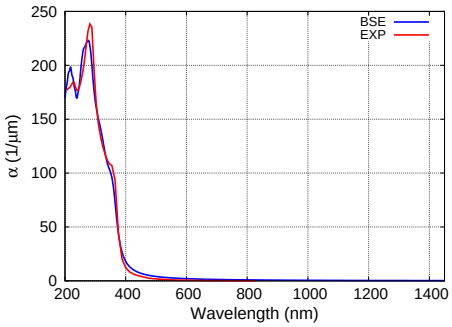


Figure 5.2: Absorption coefficient of Si calculated using BSE as compared to experimental results [1].
(courtesy of Khaled)

A summary of the obtained ab initio parameters that shall be used in the device simulations is given in table 5.2, together with the permittivity and the electron affinity that were found in [45]. The impact of the quality of the material parameters on the overall performance estimation of a particular solar cell will be discussed later on in this chapter.

It is also important to mention that in reality, the electron and hole mobilities may still vary, based on the doping concentrations and amount of defects[66].

Coming back to WxAMPS, under defects, the user can choose whether the defects states are donor-like or acceptor-like. Donor-like means the energy levels are closer to that of the conduction band energy and acceptor-like are the defects whose energy level is closer to that of the valence band energy. The density and the dispersion (discrete, banded or gaussian) of the defects can also be selected. The capture cross section of the defects can be added which explains the "sizes" of the target for the incoming carriers. The sofware allows the user to model defects states as localised states which form

a continuum inside the bandgap.

Table 5.2: Table of absorption data and other properties for Si (ab initio)

energy(eV)	wavelength(Microm)	absorption coefficient(cm-1)	other data
1,38277	0,897255509	6621,34	mobility(holes):
1,40281	0,884437664	6860,24	178
1,44289	0,859870122	7358,38	
1,48297	0,836630545	7884,44	mobility(electrons):
1,50301	0,825475546	8158,84	136
1,56313	0,793726689	9028,91	
1,58317	0,78367958	9335,53	effective mass(electrons):
1,64329	0,75500855	10309,68	0.9*m(0)
1,68337	0,737032263	11006,92	
1,72345	0,719892077	11745,89	effective mass(holes):
1,78357	0,695626188	12939,14	0.4*m(0)
1,82365	0,680337784	13796,11	
1,88377	0,658624991	15183,62	electron affinity:
1,94389	0,638255251	16706,98	4,05
2,00401	0,619107689	18383,81	
2,08417	0,595295969	20894,79	permitivity:
2,14429	0,578605506	23017,28	11,9
2,20441	0,562825427	25379,62	
2,30461	0,538354863	29956,39	Band-gap
2,38477	0,520258977	34329,47	1,24
2,48497	0,499280877	40956,6	
2,58517	0,47992898	49312,94	
2,70541	0,458598882	62658,74	
2,82565	0,439084105	81703,82	
2,94589	0,421162365	110721,24	
3,26653	0,379821401	369112,69	
3,44689	0,359947083	858025,27	
3,64729	0,340169825	1085331,99	
3,86774	0,320781128	1365257,05	
4,12826	0,300537757	1651763,63	

Results

Various types of results can be obtained with the help of WxAMPS, depending on the users' objectives. In under the results tab, the user can choose to look at IV characteristics, or at energy band levels, carrier variations across the device, electric field distribution in the device, current distribution, recombination and generation effects, carrier lifetimes and the quantum efficiency as a function of the wavelength.

5.0.1 Simulation of the silicon based P-N junction

Table 5.3: Properties of silicon at 300 K
[6]

Property	Value
Atomic density	5×10^{22} cm^{-3} or 5×10^{28} m^{-3}
Atomic weight	28.09u
Density	2.328 kg.cm^{-3} or 2.328 g.cm^{-3}
Bandgap	1.1242 eV
Intrinsic carrier concentration	1×10^{10} cm^{-3} or 1×10^{16} m^{-3}
Lattice constant	0.543095 nm
Effective density of states conduction(Nc)	3×10^{19} cm^{-3} or 3×10^{25} m^{-3}
Effective density of states valence(Nv)	1×10^{19} cm^{-3} or 1×10^{25} m^{-3}
Relative permittivity	11.7
Electron affinity	4.05 eV
Electron mobility	1350 cm^2.V^{-1}.s^{-1}
Hole mobility	480 cm^2.V^{-1}.s^{-1}

For the purpose of this work, only the effect of material properties on the IV characterics were studied with particular emphasis on the overall efficency of the solar cell device. This is done because the efficiency is arguably the most important parameter to compare the device in question against all other devices. A simple silicon based P-N juction device is chosen for the purpose of this work. The ab initio-calculated data and experimental data were chosen as input parameters, and a simulation was carried out and the results were compared. An analysis of the impact of the doping concentration using the experimental data given in table 5.3 is shown in figure 5.5, 5.6 and 5.7. The effective densities are calculated from the effective masses

using the formula:

$$N_i = 2(\frac{2\pi m_{carrier} kT}{h^2})^{\frac{3}{2}}. \tag{5.7}$$

The standard silicon absorption data that comes with the WxAMPS package is used for the "experimental" model.

The simulation results for the "ab initio-based" model (Figure 5.4) and the "experimental" model (Figure 5.3) are given below.

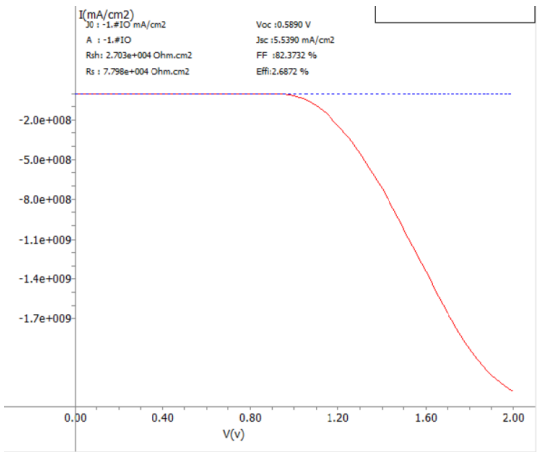


Figure 5.3: P-N junction simulation using experimental data

Experimental model: The fill factor is obtained to be 82.3732 and the efficiency is obtained to be 2.6872%.

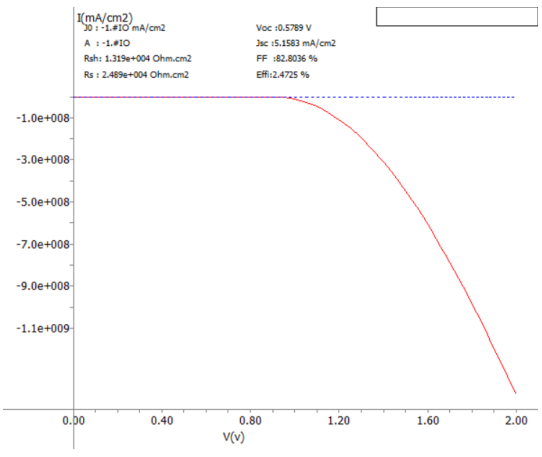


Figure 5.4: P-N junction simulation using ab initio data

ab initio model: The fill factor is obtained to be 82.8026 and the efficiency

is obtained to be 2.4725%.

The simulation output results are given below for the case of light, moderate and heavy doping concentrations using the experimental model.

Light doping

Figure 5.5 shows the IV characteristic output of the device with a doping level of 1×10^{12}.

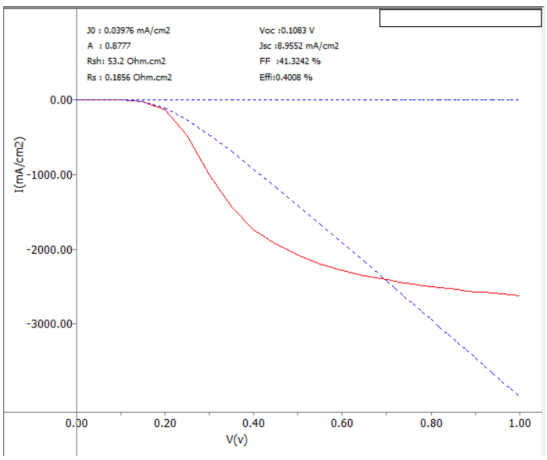


Figure 5.5: IV curve for light doping case

The fill factor of the device is 41.32 and the overall efficiency is 0.400 %.

Moderate doping

Figure 5.6 shows the IV characteristic output of the device with a doping level of 1×10^{15}.

The fill factor of the device is 69.70 and the overall efficiency is 3.00 %.

Heavy doping

Figure 5.7 shows the IV characteristic output of the device with a doping level of 1×10^{19}.

The fill factor of the device is 78.94 and the overall efficiency is 2.78 %.

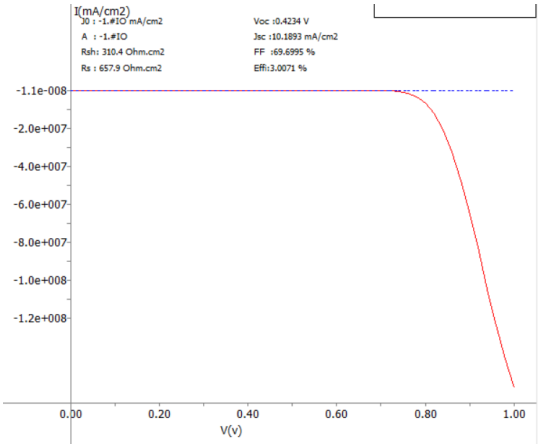


Figure 5.6: IV curve for the moderate doping case

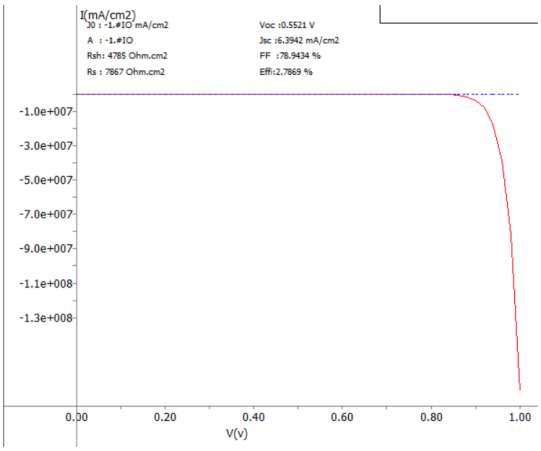


Figure 5.7: IV curve for the heavy doping case

5.0.2 Discussion

In the results obtained from the simulation, it is clear that one can easily model solar cells using a either ab initio data or experimental data or even a combination of both. Other parameters except those shown in table 5.2 and 5.3 were kept fixed when comparing the ab initio and the experimental model simulations. The efficiencies for both, the ab initio model and the experimental model were $\approx 2.5\%$ which ascertains the quality of the ab initio data for the estimation of device performance. The slight difference ($\approx 0.1\%$) is due to the mobilites being too low for the ab initio model. This error is driven by the accuracy of the curvature of the bands and the estimation of the effective masses, together with the estimation of the computed relaxation

time. The use of ab initio simulations are a useful tool for the development of new materials, or the modification of existing device designs.

WxAMPS contains a standard case file for silicon where they have modeled p-i-n silicon device and although this device has unique properties as a result of some of the parameters used such as layer thicknesses and doping levels, the values used for this simulation can be used as a base to test the impact of device parameters such as doping on the performance of the device. The case file generates an efficiency of ≈2.8%, which ascertains the accuracy of the result of our modeled device.

The simulation result in figure 5.6 is for a simple P-N junction where both the p-type layer and the n-type layer are moderately doped ($1\times10^{19}\text{cm}^{-3}$). The doping of the layers introduces impurities, which are also defects.

Increasing the doping concentration reduces the mobility of the carriers and vice versa. It is also known that introducing a huge concentration of dopants greately disturbs the semiconductor system, resulting in bandgap reductions and affecting the efficiency which is what we can see from our result. It is also clear that reducing the doping significantly will affect the carrier concentration as with the lightly doped case, and the open circuit voltage is reduced which affects the overall efficiency of the solar cell. Increasing the doping concentration is not always beneficial. However, moderate doping values are optimal for performance improvement. For values around the moderate doping concentration, a higher doping level leads to a lower resistance and a higher open circuit voltage. This results in a higher efficiency of the solar cell.

5.1 Summary

This chapter has demonstrated how device simulations are done. A comparison of using experimental or ab initio calculated data has been done. The impact of device parameters on the performance of a device has also been studied. Chapter 6 shall explore the use of frequency conversion techniques for solar cell device modelling applications.

Chapter 6

Frequency conversion

In the following chapter, the proposition of using a frequency conversion process for solar cells is explained and the modelling of such a process in the context of solar cells is also discussed.

6.1 Up-conversion

In the case of solar cells, Up-conversion (UC) is a process in which the sub-band-gap photons are transmitted into high-energy photons that can then be absorbed by the solar cell and be utilized to produce electron-hole pairs[67]. In the case of crystalline silicon device for example, the 20 percent of the solar spectrum with energy lower than the bandgap energy can be upconverted by an up-conversion layer situated at the rear of the device and improve the overall solar cell spectral response. An UC process entails the absorption of two or more photons in the sub-band-gap spectrum range (long wavelengths), and a subsequent emission of a photon in the visible spectrum where the photon can be utilized in the photo-conversion process and contribute to current generation. The UC process makes use of a luminescent material(phosphor) that has multiple energy levels with favourable energy level spacings. This premise makes lanthanide ions such as Er^{3+} (trivalent erbium), or Er^{3+} co-doped with ytterbium[68] very attractive for the use in UC applications[69][70]. Doping optical materials with one or more of these activator ions, with the inclusion of sensitizer ions such as Yb^{3+} as co-dopants is one of the many methods being explored in literature for several up-conversion applications[71][72]. Co-dopants that are added are used to increase the overall absorption cross section through energy transfer and thus improve the UC efficiency[72].Energy transfer up-conversion (ETU) is the result of successive energy transfers between ions at different sites through

mutual interactions. The first ion to be excited is called a sensitizer and the ion to which energy is transferred is called the activator.

6.2 Down-conversion

Another frequency conversion technique that can be applied is down-conversion (DC). DC is the conversion of high energy photons into lower energy photons that can be absorbed and utilized in the photo-conversion process, thus reducing thermalization losses. Methods such as multiple electron-hole pair generation from one high energy photon are being explored[67].

To understand the nature of frequency conversion and all the relevant interactions and processes that are involved, a rate equation model as proposed by Fischer et al[71] is used with an emphasis on the simulations of such processes in the context of solar cells. This model takes into consideration all relevant the processes involved such as ground state absorption(GSA), spontaneous emission(SPE), excited state absorption(ESA), stimulated emission(STE), multi-phonon relaxation(MPR) and energy transfer(ET).

6.2.1 The general rate equation model

In the rate equation model a general occupation vector $\vec{n}$ is used to describe the occupation of the energy levels under consideration for a specific system. The individual components of the vector each describe the relative occupation of an energy level. Therefore, the number of excited ions in a given energy level N_j is described by[71],

$$N_j = n_j \rho_{Er}. \tag{6.1}$$

Here, the density of the lanthinide ions in the host material is given by ρ_{Er} and n_j denotes the relative occupation of a particular energy level j.

The rate at which the occupation of the energy levels is changing is described by the general differential equation[71]:

$$\dot{\vec{n}} = \left[M_{GSA} + M_{STE} + M_{ESA} + M_{SPE} + M_{MPR}\right] \vec{n} + \vec{\nu}_{ET}(\vec{n}) \tag{6.2}$$

All of the processes linear to the occupation vector $\vec{n}$ are described by matrices[71]. The ground state absorption is described by the matrix M_{GSA}, M_{ESA} denotes excited state absorption, M_{STE} denotes stimulated emission. M_{SPE} gives the contribution from the spontaneous emission and M_{MPR} denotes the contribution from multi-phonon relaxation. $\vec{\nu}_{ET}(\vec{n})$ is the term that describes the energy transfer and cross relaxation processes. It not linear with $\vec{n}$. The probabilities describing each of the matrix elements for each of the processes except for MPR processes can be described by their respective Einstein coefficients, which can either be obtained from experimental data or calculated from the Judd-Ofelt theory (JO)[73][74]. The attractiveness of the JO theory is that it allows us to easily compute oscillator strengths in absorption and luminescence, luminescence branching ratios, excited-state radiative life-times, intensity parameters and transition probabilities[72].

6.2.2 Photon absorption and emission

To calculate the photon flux derived from the frequency conversion process, a system with an incoming number of photons (N_p) with an energy $E_{ab} = \hbar\omega_{ab}$ can be considered. The density of the number of atoms in the ground state and the excited state are given by N_a and N_b with energies E_a and E_b, respectively. The total photon emission is equal to the stimulated and spontaneous emission and is given by:

$$\left(\frac{dN_p}{dt}\right)_{total} = \left(\frac{dN_p}{dt}\right)_{spontaneous} + \left(\frac{dN_p}{dt}\right)_{stimulated} = AN_b + BN_bN_p. \quad (6.3)$$

Here, A is the Einstein coefficient for the spontaneous emmision process and B is the Einstein coefficient for the stimulated emission process. In the case of photovoltaic applications, the stimulated emmision is not relevant and the above equation becomes,

$$\left(\frac{dN_p}{dt}\right)_{spontaneous} = AN_b = \frac{1}{\tau_b}N_b \quad (6.4)$$

where τ_b is the radiative lifetime of an arbitrary state b and N_b is the population density of that arbitrary state from which the electrons decay to a lower electronic state to release an up- or down- converted photons. The total photon flux intensity $\phi_{ex}(\lambda)$ obtained over the material sample length d can then be estimated by,

$$\phi_{ex}(\lambda) = \frac{1}{\tau_b}N_b d\ g(\lambda, \lambda_0) = \phi_{econversion}(\lambda). \quad (6.5)$$

Here, $g(\lambda, \lambda_0)$ is the line shape function that is just a constant.

6.2.3 Generation rate and photocurrent density

The generation rate G_{ex} resulting from the up conversion is estimated by

$$G_{ex} = \alpha(\lambda)\phi_{conversion}. \quad (6.6)$$

The current density term that accounts for the short circuit contributions to the total generation rate from the up-conversion layer is added to the solar cell current density. This extra current density contribution produced by a single line emission at (λ_0) by the up-conversion material layer can be estimated by:

$$J_{ex} = q(1 - R(\lambda))\ G_{ex}(\lambda_0)\ L. \quad (6.7)$$

Here, L is the effective layer thickness. $\alpha(\lambda_0)$ is the absorption coefficient of the up-converted photons and $\phi_{conversion}$ is the photon flux density from the conversion material layer.

6.3 Up-conversion results

6.3.1 Energy scheme and rate equations for Er^{3+} co-doped with Yb^{3+}

Phosphors with trivalent erbium (Er^{3+}) co-doped with ytterbium(Yb^{3+}) offer a desirable efficiency gain due to the Erbium's favourable photo-luminescence within the visible spectrum. The cross section of Yb^{3+} is 10X that of Er^{3+} for some of the infrared energies making it a good sensitizer for Er^{3+}[75]. Figure 6.1 shows the energy transfer processes in the co-doped system. The σ_{if} denote the emission and absorption cross sections, and W_{if} is the spontaneous decay rates. i and f denote the ititial and final states, respectively. The energy transfer rates are shown by C_{ij}, where i and j are the donor and acceptor energy levels, respectively. The dashed arrows indicate the instantaneous processes such as MPR. The system is explained by 9 equations which are solved simultaneously for the populations of the 7 energy levels. The rate equations are given by[75]

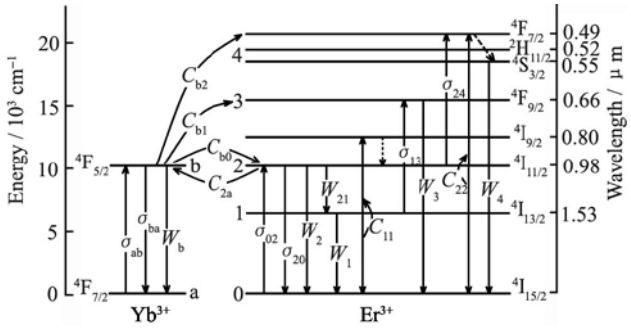


Figure 6.1: Energy scheme of Er^{3+} co-doped with Yb^{3+}
(Sourced from [75])

$$\frac{dN_a}{dt} = -\sigma_{ab}\phi_p N_a + \sigma_{ba}\phi_p N_b + W_b N_b \tag{6.8}$$

$$\begin{aligned}\frac{dN_b}{dt} = \; & \sigma_{ab}\phi_p N_a - \sigma_{ba}\phi_p N_b - W_b N_b + \\ & C_{2a} N_a N_2 - C_{b0} N_b N_0 - C_{b1} N_b N_1 - C_{b2} N_b N_2\end{aligned} \tag{6.9}$$

$$N_{Yb} = N_a + N_b \tag{6.10}$$

$$\begin{aligned}\frac{dN_0}{dt} = &- \sigma_{02}\phi_p N_0 + \sigma_{20}\phi_p N_2 + W_1 N_1 + C_{11} N_1 N_2 \\ &+ C_{22} N_2^2 + W_3 N_3 + W_4 N_4\end{aligned} \tag{6.11}$$

$$\frac{dN_1}{dt} = W_{21} N_2 - W_1 N_1 - C_{b1} N_b N_1 - 2C_{11} N_1^2 - \sigma_{13}\phi_p N_1 \tag{6.12}$$

$$\begin{aligned}\frac{dN_2}{dt} = &\ \sigma_{02}\phi_p N_0 - \sigma_{20}\phi_p N_2 - W_2 N_2 + C_{11} N_1^2 \\ &- 2C_{22} N_2^2 + C_{b0} N_b N_b N_0 - C_{2a} N_a N_2 - C_{b2} N_b N_2\end{aligned} \tag{6.13}$$

$$\frac{dN_3}{dt} = \sigma_{13}\phi_p N_1 - W_3 N_3 + C_{b1} N_b N_1 \tag{6.14}$$

$$\frac{dN_4}{dt} = \sigma_{24}\phi_p N_2 - W_4 N_4 + C_{22} N_2^2 + C_{b2} N_b N_2 \tag{6.15}$$

$$N_{Er} = N_0 + N_1 + N_2 + N_3 + N_4. \tag{6.16}$$

In the equations above, N_i denotes the population density of the energy level i and ϕ_p denotes the photon flux density of the pump wavelength.

6.3.2 Results

Table 6.1: Parameters used for the Er/Yb system calculations [76, 77, 75]

Parameters	Symbol	Value
Pump wavelength	λ_p	980 nm
Er concentration	N_{Er}	
Yb concentration	N_{Yb}	
Absorption cross section Yb^{3+} $^2F_{5/2}$ at λ_p	σ_{ab}	1.30×10^{-20} cm^2
Emission cross section Yb^{3+} $^2F_{5/2}$ at λ_p	σ_{ba}	1.30×10^{-20} cm^2
Absorption cross section Er^{3+} $^4I_{11/2}$ at λ_p	σ_{02}	1.27×10^{-21} cm^2
Emission cross section Er^{3+} $^4I_{11/2}$ at λ_p	σ_{20}	1.27×10^{-21} cm^2
Decay rate of Yb^{3+} $^2F_{5/2}$	W_b	
Decay rate of Er^{3+} $^4I_{13/2}$	W_1	
ESA cross section Er^{3+} $^4I_{13/2}$ at λ_p	σ_{13}	1×10^{-22} cm^2
ESA cross section Er^{3+} $^4I_{11/2}$ at λ_p	σ_{24}	1×10^{-22} cm^2
Decay rate of Er^{3+} $^4I_{11/2}$	W_2	40000 s^{-1}
Transition rate Er^{3+} $^4I_{11/2}\rightarrow{}^4I_{13/2}$	W_{21}	5000 s^{-1}
Decay rate of Er^{3+} $^4F_{9/2}$	W_3	500000 s^{-1}
Decay rate of Er^{3+} $^4S_{3/2}$	W_4	100000 s^{-1}
Energy transfer rate $Yb^{3+}\rightarrow Er^{3+}$ 0 ($^2F_{5/2}+{}^4I_{15/2}\rightarrow{}^2F_{7/2}+{}^4I_{11/2}$)	C_{b0}	4×10^{-17} cm^3/s
Energy transfer rate $Yb^{3+}\rightarrow Er^{3+}$ 1 ($^2F_{5/2}+{}^4I_{13/2}\rightarrow{}^2F_{7/2}+{}^4F_{9/2}$)	C_{b1}	4×10^{-18} cm^3/s
Energy transfer rate $Yb^{3+}\rightarrow Er^{3+}$ 2 ($^2F_{5/2}+{}^4I_{11/2}\rightarrow{}^2F_{7/2}+{}^4F_{7/2}$)	C_{b2}	4×10^{-17} cm^3/s
Energy transfer rate $Er^{3+}\rightarrow Yb^{3+}$ ($^2F_{7/2}+{}^4I_{11/2}\rightarrow{}^2F_{5/2}+{}^4I_{15/2}$)	C_{2a}	4×10^{-17} cm^3/s
Cooperative upconversion coefficient 1 Er^{3+}($^4I_{13/2}+{}^4I_{13/2}\rightarrow{}^4I_{9/2}+{}^4I_{15/2}$)	C_{11}	4×10^{-18} cm^3/s
Cooperative upconversion coefficient 2 Er^{3+}($^4I_{11/2}+{}^4I_{11/2}\rightarrow{}^4F_{7/2}+{}^4I_{15/2}$)	C_{22}	2×10^{-18} cm^3/s

The set of equations are solved in the steady state with $\frac{dN_i}{dt} = 0$ using Matlab for the different population densities. All the parameters in the equations are given in table 6.1. The photon flux density used in the calculation is obtained by integration of the solar spectrum around the infrared wavelengths for the up-conversion material. In the case of the Er/Yb co-doped system, the pump wavelength is 980 nm. The corresponding photon flux is calculated using $\phi_p = \frac{I \times \lambda}{E}$, where I is the spectral irradiance, λ the pump wavelength and E the photon energy. The pump photon flux was obtained to be $\phi_p = 1.22 \times 10^{17} \mathrm{cm}^{-2} \mathrm{s}^{-1}$

Table 6.2: Population densities of the energy levels (Er/Yb system)

Parameter	**Result**
N_a	1.5×10^{20} cm^{-3}
N_b	7.5×10^{-21} cm^{-3}
N_0	2.5×10^{20} cm^{-3}
N_1	3.8×10^{14} cm^{-3}
N_2	6.4×10^{13} cm^{-3}
N_3	7.6×10^{6} cm^{-3}
N_4	6.4×10^{6} cm^{-3}

The population densities N_i are given in the table 6.2 as obtained through the computation of the steady state rate equations. $N_{Er} = 2.6 \times 10^{20} \mathrm{cm}^{-3}$ and $N_{Yb} = 10 \times 10^{20} \mathrm{cm}^{-3}$. Of particular interest for up-conversion applications in solar cells is the population density of the energy level N_4 and N_3 which results in photon emission around 550 nm and 660 nm, respectively, for electron transitions to the ground state. The emitted photon flux is

$$\phi_{conversion} = \frac{1}{\tau_i} N_i d g(\lambda, \lambda_0), \tag{6.17}$$

Where d is chosen to be 2000 nm which is a thin film rather than a bulk glass layer, and $g(\lambda, \lambda_0)$ is a line shape function which is taken to be 1. In this example, $\frac{1}{\tau}$ is given by the decay rate denoted by W_i, where i denotes the respective transition to the ground state. The photon flux densities resulting from the up- conversion layer related to the 550nm and the 660 nm peaks are found to be:
$\phi_{conversion}(550) = 128 \times 10^{6} \mathrm{cm}^{-2} \mathrm{s}^{-1}$

$\phi_{conversion}(660) = 640 \times 10^6 \text{cm}^{-2}\text{s}^{-1}$

To See the effect of the simulated up-conversion layer on the efficiency of a solar cell device, a simple c-Si solar cell device is simulated using WxAMPS. A standard silicon-based device case file is chosen that comes standard with the WxAMPS package since what we interested in is the overall efficiency change. The device is simulated with and without the contribution from the UC photon flux density. The photon flux density for the 980nm is set to 0 for the case with the UC since we assume all the photons around that wavelength will be transmitted. The photon flux densities for the 550 nm and 660 nm are adjusted accordingly.

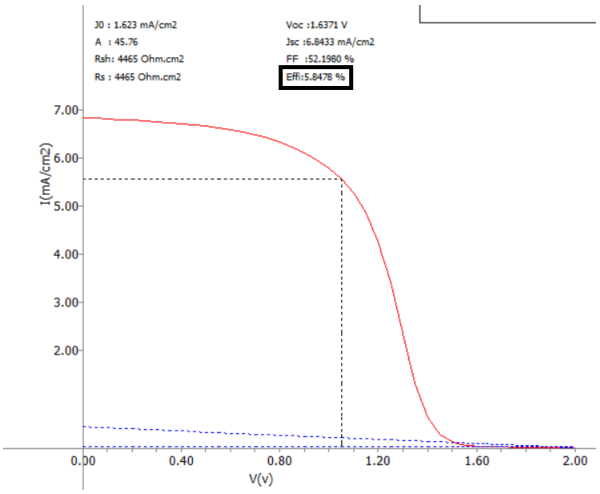


Figure 6.2: Simulation result without UC (Er/Yb system)

Figure shows the IV characteristic of the simulated device with and without UC. Table 6.3 shows the summary of the results for V_{OC}, FF and the efficiency for the device with and without UC.

The overall increase in efficiency is 0.0046% for the Er^{3+}/Yb^{3+} system.

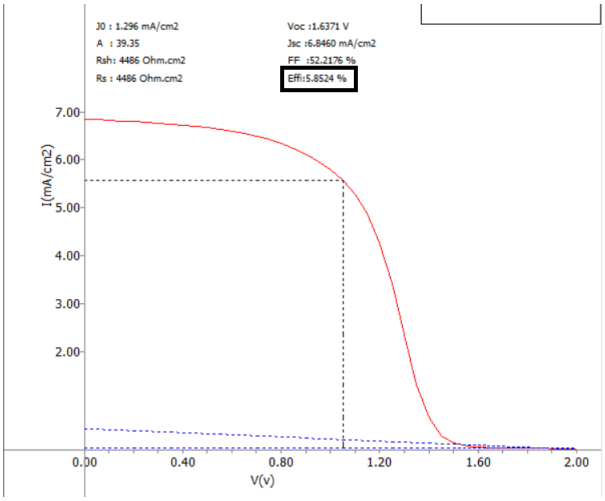


Figure 6.3: Simulation result with UC (Er/Yb system)

Table 6.3: Summary of UC results (Er/Yb system)

Parameter	Without UC	With UC
Efficiency	5.8478 %	5.8524%
Fill factor (FF)	52.1980 %	52.2176%
Short circuit current J_{sc}	6.8433 mA/cm^2	6.8460 mA/cm^2
Open circuit voltage V_{oc}	1.6371 V	1.6371 V

6.3.3 Energy scheme and rate equations for trivalent thulium (Tm^{3+}) system

The Tm^{3+} system is given in figure 6.4 with all the relevant electronic transitions which is pumped at an inuput wavelength of 1064 nm, having up-conversion emmissions of 800 nm, 750 nm and 480 nm, respectively. The pumping transitions are denoted by W_i and A_{ij} denotes the decay rate from energy level i to energy level j.

The steady state rate equations are given by[78]:

$$0 = -W_1N_0 + A_{10}N_1 + A_{30}N_3 + A_{50}N_5 \tag{6.18}$$

$$0 = W_2N_1 + W_sN_1 - A_{10}N_1 + A_{21}N_2 + W_5N_3 \tag{6.19}$$

$$0 = W_1N_0 - A_{21}N_2 + A_{52}N_5 \tag{6.20}$$

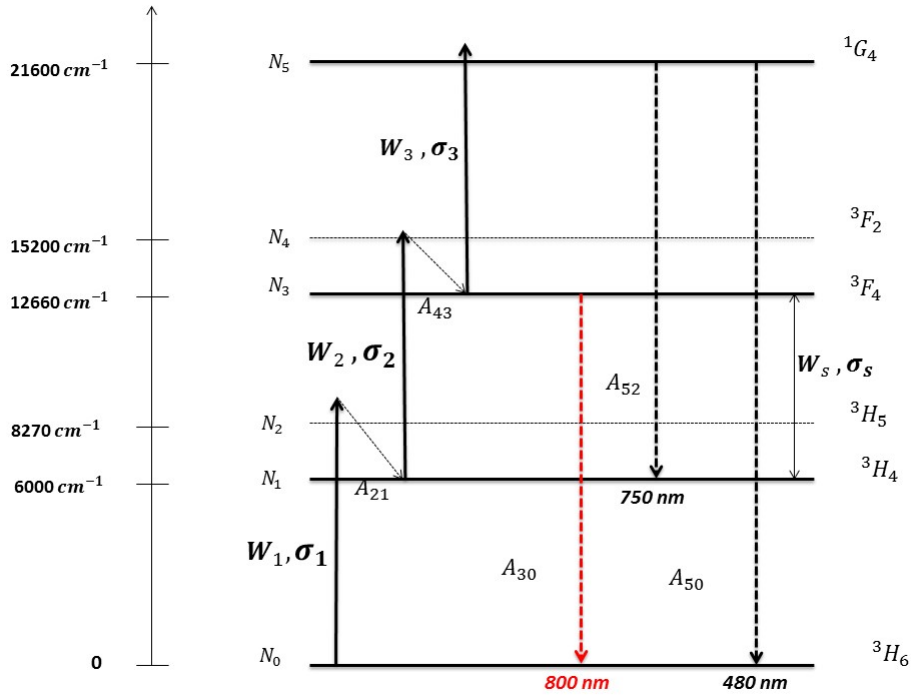


Figure 6.4: Energy scheme of Tm^{3+}
(Courtesy of Tahir)

$$0 = W_s N_1 - A_{30} N_3 - W_S N_3 + W_3 N_3 + A_{43} N_4 \tag{6.21}$$

$$0 = W_2 N_1 - A_{43} N_4 \tag{6.22}$$

$$0 = W_3 N_3 - A_{50} N_5 + A_{52} N_5 \tag{6.23}$$

$$N_{Tm^{3+}} = N_0 + N_1 + N_2 + N_3 + N_4 + N_5. \tag{6.24}$$

The parameters used for the calculation are obtained in table 6.4 .The pump transitions are determined using $W_i = \frac{P_p \sigma_i}{h v_i A_{eff}}$, where v_i is the pump frequency and A_{eff} is the effective cross section.

6.3.4 Results

The corresponding population densities for the relevant energy levels are given in table 6.5.

The extra photon flux generated from this system is obtained to be:
$\phi_{ex}(800) = 3.6 \times 10^{14} \mathrm{cm}^{-2} \mathrm{s}^{-1}$

Table 6.4: Parameters used for Tm^{3+} rate equations calculations

Parameter	**Symbol**	**Value**
GSA cross section	σ_1	1.1×10^{-25} m^{-3}
ESA_1 cross section	σ_2	8.2×10^{-23} m^{-3}
ESA_2 cross section	σ_3	1.0×10^{-24} m^{-3}
Stimulated cross-section	σ_s	6.7×10^{-23} m^{-3}
Decay rate from level 1 to 0	A_{10}	108.6 s^{-1}
Decay rate from level 3 to 0	A_{30}	594.6 s^{-1}
Decay rate from level 5 to 0	A_{50}	491.8 s^{-1}
Decay rate from level 5 to 2	A_{52}	384.4 s^{-1}
Pump wavelength	λ_p	1064 nm
Total Tm^{3+} concentration	$N_{Tm^{3+}}$	8×10^{26} m^{-3}
Effective cross section	A_{eff}	0.5×0.5 mm^3
Pump power	P_p	0.2 W
Material thickness	d	2000 nm

Table 6.5: Population densities of the energy levels for Tm^{3+}

Parameter	**Result**
N_0	8×10^{26} m^{-3}
N_1	3.3×10^{22} m^{-3}
N_3	2×10^{19} m^{-3}
N_5	9.6×10^{15} m^{-3}

Figure 6.5 and 6.6 show the simulation results for the case without UC and with UC, respectively.

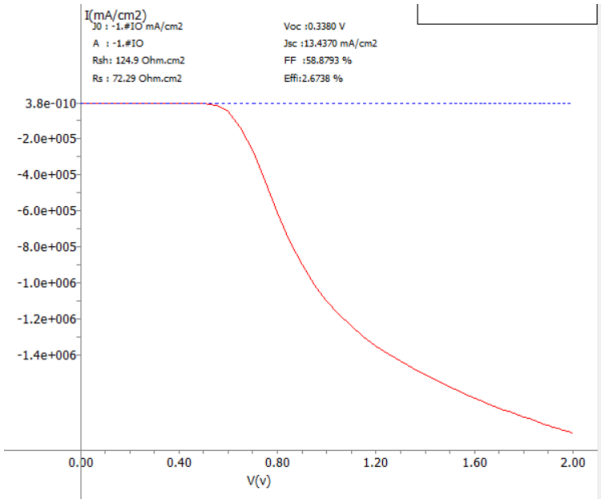


Figure 6.5: Simulation result without UC (Th^{3+} system)

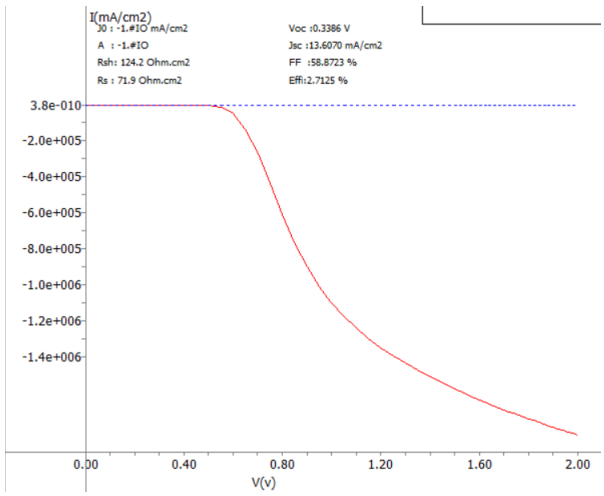


Figure 6.6: Simulation result with UC (Tm^{3+} system)

Table 6.6 shows the summary of the results for V_{OC}, FF and the efficiency for the device with and without UC.

The overall increase in efficiency is 0.0387% for the Er^{3+}/Yb^{3+} system.

Table 6.6: Summary of UC results (Thulium system)

Parameter	Without UC	With UC
Efficiency	2.6738 %	2.7125%
Fill factor (FF)	58.8793 %	58.8723%
Short circuit current J_{sc}	13.4370 mA/cm^2	13.6070 mA/cm^2
Open circuit voltage V_{oc}	0.3380 V	0.3386 V

6.3.5 Discussion

It has been shown that a simple UC simulation can be done using experimental or calculated parameters. Two systems were used to demonstrate the concept. The first case was for a material containing erbium co-doped with ytterium, and the second case was for a thulium doped material. However, it should be noted that one can do a similar analysis with any UC material, where the material is pumped at any wavelength. Also, a material layer system with a variety of lanthinide ions all pumping at different wavelengths could be modelled and analysed in a bid to harness more infrared photons. Down-conversion from the UV to the visible part of the solar spectrum can also be computed.

From the rate equations, the concentration of the lanthinide ions is an important factor affecting the number of photons that are transmitted. The lower the concentration, the lower the population density of each energy level, which reduces the resultant photon flux intensity. This in turn reduces the generation rate and the resultant cell efficiency. The line shape function was taken to be one but a more accurate estimation can be done using the approximation for the FWHM approximation which is given by FWHM$\approx 2.334\sigma$ where σ is the standard diviation from the output wavelength. Due to the high orders of magnitude for the other variables in the calculation of the photon flux density, the effect of the line shape function on the overall photon flux density is negligible.

The impact of the UC photons was as expected since we had an overall increase in efficiency of 0.0046% for the Er^{3+}/Yb^{3+} system and 0.0387% for the Tm^{3+} system. It is clear that although both systems result in efficiency increases, the Er/Yb system is less efficient in UC. This might be due to the inefficiencies of the energy transfer processes between the sensitisor and the activator.

The WxAMPS package uses photon waveleghths that go up in increments of 20 nm so the impact of the distribution of the peak around the UC wavelengths cannot be well accounted for, which might result in a slight increase in the efficiency change if included. The dependence of the efficiency on the material size should also be considered since a very thick material can result in a high efficiency. Using a systematic increase in the size of the UC layer, one can estimate the size of a glass layer that would result in practical increases of the efficiency of 1%, but we did not want to give the false impression that the present methods are already perfect. With a thicker layer, we also have to take into account Beer‘s law, which reduces the efficiency of the UC layers, and strongly depends on doping.

Also, the UC material layer is modelled as isolated from the solar cell but the layer is indeed coupled to the solar cell device and recombination effects at the contacts, backreflection and other factors might lead to spectral losses and affect the efficiency. Furthermore, defects in the UC material might lead to the reduction in the number of photons that are being transmitted.

6.4 Summary

This chapter has explained the main formalism for the implementation of up-conversion and down-conversion in solar cells. Detailed examples have been shown to illustrate the principal usefulness of this tool.

Chapter 7

Conclusions and future work

7.1 Conclusions

In this work, it has been shown that it is possible to generate device simulations using ab initio and experimental data, and extract various types of results for device performance analysis. The effect of certain device parameters on the overall device performance was discussed. The results have shown that the estimation of the device performance from ab initio data produces close to accurate results since both the device modelled from the ab initio data and the one modelled from experimental data yielded efficiencies of $\approx$ 2.5%. This can serve as a useful tool in the development of new or improved solar cell devices using promising new types of materials. We have shown that the implentation of frequency conversion techniques within the device simulations is possible, and can in combination with experimental studies, be used as a basis for the development of novel solar cells that include such techniques. The positive effect of UC on the solar cell device performance has been shown for two different types of rare earth material systems.

7.2 Future work

The modeling and simulation of materials of other solar cell materials such as CdTe and Perovskites would be interesting, as many groups worldwide study such materials[79, 80, 81], including Tandem cells can be designed and the effects of various parameters on the overall device performance can be studied. Ab initio data sets of more materials can be produced for extended databases, which allow for simulations that accompany experimental work. Frequency conversion with multiple rare-earth material systems, or other

systems such as quantum dots can be studied to see the overall impact on device performance. One can also systematically search for systems where the transitions occur close to the band gap energies and which should have the best efficiencies.

Conferences/workshops attended

- PLESC international workshop, titled "Plasmonics and nanoantennas for solar cells", held on 09/05/2017 at University of the Witwatersrand, Johannesburg.
- MERG annual workshop, held on 01/11/2017-02/11/2017 at Societa Dante Alighieri, Johannesburg.
- DST-NRF CoE-SM/AMSEN annual student Presentation, poster entitled "Solar cell device simulations and the implementation of frequency conversion techniques", held on 04/04/2018 at the University of the Witwatersran, Johannesburg.

Publications

- I. Mokgosi, T. Aslan, R. Warmbier and A. Quandt, "Solar cell device simulations", *Transparent Optical Networks (ICTON).* IEEE Xplore, Spain, 2017.
- I. Mokgosi, T. Aslan, R. Warmbier and A. Quandt,"Advanced light harnessing features in solar cell device simulations", *Transparent Optical Networks (ICTON).* IEEE Xplore, Spain, 2018.
- I. Mokgosi, T. Aslan, R. Warmbier, A. Quandt, M. Ferrari and G.Righini, "About the implementation of up -conversion processes in solar cell simulations", *Glassy Materials Based Microdevices.* MDPI, Switzerland, 2018.

Bibliography

[1] D. Aspnes and A. Studna, "Dielectric functions and optical parameters of Si, Ge, GaP, GaAs, GaSb, InP, InAs, and InSb from 1.5 to 6.0 eV," *Phys. Rev. B*, vol. 27, no. 2, p. 985, 1983.

[2] A. Fahrenbruch and R. Bube, *Fundamentals of solar cells: photovoltaic solar energy conversion*. Elsevier, Cambridge, 2012.

[3] V. Balzani and N. Armaroli, *Energy for a sustainable world: from the oil age to a sun-powered future*. John Wiley & Sons, New York, 2010.

[4] P. Wiirfel *et al.*, *Physics of solar cells: from principles to new concepts*. John Wiley & Sons, New York, 2008.

[5] E. Becquerel, "On electric effects under the influence of solar radiation," *Compt. Rend.*, vol. 9, p. 561, 1839.

[6] M. Green, "Solar cells: operating principles, technology, and system applications," 1982.

[7] G. Boyle *et al.*, *Renewable energy: power for a sustainable future*. Taylor & Francis, Oxford, 1997.

[8] S. Fonash, *Solar cell device physics*. Elsevier, New York, 2012.

[9] C. Kittel, *Introduction to solid state physics*. Wiley, New York, 2005.

[10] TUdelft, "Semiconductor materials for solar cells," 2016. retrieved from https://ocw.tudelft.nl/, [accessed 13-June-2017].

[11] F. Lindholm, J. Fossum, and E. Burgess, "Application of the superposition principle to solar-cell analysis," *IEEE Transactions on Electron Devices*, vol. 26, no. 3, pp. 165–171, 1979.

[12] J. Hamilton, "Careers in solar power," 2013. retrieved from https://www.bls.gov/green/solarpower, [accessed 13-June-2017].

[13] PVeducation, "I-v curves," 2016. retrieved from http://pveducation.org/, [accessed 13-June-2017].

[14] J. Fossum, "Computer-aided numerical analysis of silicon solar cells," *Solid-State Electronics*, vol. 19, no. 4, pp. 269–277, 1976.

[15] W. Shockley and H. Queisser, "Detailed balance limit of efficiency of p-n junction solar cells," *Journal of applied physics*, vol. 32, no. 3, pp. 510–519, 1961.

[16] S. Fonash, J. Arch, J. Cuiffi, J. Hou, W. Howland, P. McElheny, A. Moquin, M. Rogossky, F. Rubinelli, T. Tran, *et al.*, "A manual for amps-1d for windows 95/nt," *The Pennsylvania State University*, pp. 10–31, 1997.

[17] J. Pala, M. Mordiya, D. Virpariya, A. Dangodara, P. Gandha, C. Savaliya, J. Joseph, T. Shiyani, D. Dhruv, and J. Markna, "Analysis and design optimization of organic dye sensitized solar cell based on simulation," in *AIP Conference Proceedings*, vol. 1837, p. 030004, AIP Publishing, 2017.

[18] A. Luque and S. Hegedus, *Handbook of photovoltaic science and engineering*. John Wiley & Sons, New York, 2011.

[19] M. Rudan, *Physics of semiconductor devices*. Springer, Germany, 2016.

[20] A. Smets, K. Jäger, O. Isabella, R. Van Swaaij, and M. Zeman, *Solar Energy: The physics and engineering of photovoltaic conversion, technologies and systems*. UIT Cambridge Limited, Cambridge, 2016.

[21] U. Woggon, *Optical properties of semiconductor quantum dots*. Springer, Germany, 1997.

[22] L. Schiff, "Quantum mechanics 3rd," *New York: M cGraw-Hill*, pp. 61–62, 1968.

[23] D. Griffiths, *Introduction to quantum mechanics*. Cambridge University Press, Cambridge, 2016.

[24] P. Wiirfel, *Physics of Solar Cells*. John Wiley & Son, New York, 2005.

[25] N. Ashcroft and N. Mermin, *Solid state physics*. Saunders college, Philadelphia, 1976.

[26] S. Sze and Others, *Physics of semiconductor devices*. John wiley & sons, New York, 2006.

[27] M. Parker, *Solid State and Quantum Theory for Optoelectronics*. CRC Press, Florida, 2009.

[28] R. Pierret, *Semiconductor device fundamentals*. Pearson Education India, India, 1996.

[29] C. Brabec, "Semiconductor aspects of organic bulk heterojunction solar cells," in *Organic Photovoltaics*, pp. 159–248, Springer, 2003.

[30] J. Pankove, *Optical processes in semiconductors*. Courier Corporation, Massachusetts, 1971.

[31] Q. Hu, C. Mears, P. Richards, and F. Lloyd, "Quantum susceptance and its effects on the high-frequency response of superconducting tunnel junctions," *Physical Review B*, vol. 42, no. 16, p. 10250, 1990.

[32] M. Fukuda, *Optical semiconductor devices*, vol. 46. John Wiley & Sons, New York, 1999.

[33] X. Tong, *Advanced materials for integrated optical waveguides*. Springer, Germany, 2016.

[34] M. Abdelhameed, M. Abdelaziz, and A. Bayoumi, "Enhancement of the output power generated from a hybrid solar thermal system," *Int. J. Res. Eng. Technol.*, vol. 3, no. 1, pp. 322–334, 2014.

[35] R. Neville, *Solar energy conversion: the solar cell*. Elsevier, New York, 1995.

[36] R. Pierret and G. Neudeck, *Advanced semiconductor fundamentals*, vol. 6. Addison-Wesley Reading, Boston, 1987.

[37] H. Lee, *Thermal design: heat sinks, thermoelectrics, heat pipes, compact heat exchangers, and solar cells*. John Wiley & Sons, New York, 2010.

[38] S. Durbin and J. Gray, "Numerical modeling of photon recycling in solar cells," *IEEE Transactions on Electron Devices*, vol. 41, no. 2, pp. 239–245, 1994.

[39] M. Lundstrom and R. Schuelke, "Modeling semiconductor heterojunctions in equilibrium," *Solid-State Electronics*, vol. 25, no. 8, pp. 683–691, 1982.

[40] R. Pierret, *Modular series on solid state devices*. Addison-Wesley, Boston, 1983.

[41] W. Roosbroeck, "Theory of the flow of electrons and holes in germanium and other semiconductors," *Bell Labs Technical Journal*, vol. 29, no. 4, pp. 560–607, 1950.

[42] S. Saha, *Compact Models for Integrated Circuit Design: Conventional Transistors and Beyond*. CRC Press, Florida, 2016.

[43] A. McEvoy, T. Markvart, L. Castañer, T. Markvart, and L. Castaner, *Practical handbook of photovoltaics: fundamentals and applications*. Elsevier, New York, 2003.

[44] R. Sinton and A. Cuevas, "Contactless determination of current–voltage characteristics and minority-carrier lifetimes in semiconductors from quasi-steady-state photoconductance data," *Applied Physics Letters*, vol. 69, no. 17, pp. 2510–2512, 1996.

[45] M. Green, "Solar cell fill factors: General graph and empirical expressions," *Solid-State Electronics*, vol. 24, no. 8, pp. 788–789, 1981.

[46] M. Burgelman, J. Verschraegen, S. Degrave, and P. Nollet, "Modeling thin-film pv devices," *Progress in Photovoltaics: Research and Applications*, vol. 12, no. 2-3, pp. 143–153, 2004.

[47] H. Zhu, A. Kalkan, J. Hou, and S. Fonash, "Applications of amps-1d for solar cell simulation," in *AIP Conference Proceedings*, vol. 462, pp. 309–314, AIP, 1999.

[48] Y. Liu, Y. Sun, and A. Rockett, "A new simulation software of solar cellswxamps," *Solar Energy Materials and Solar Cells*, vol. 98, pp. 124–128, 2012.

[49] D. Clugston and P. Basore, "Pc1d version 5: 32-bit solar cell modeling on personal computers," in *Photovoltaic Specialists Conference, 1997., Conference Record of the Twenty-Sixth IEEE*, pp. 207–210, IEEE, 1997.

[50] M. Burgelman, P. Nollet, and S. Degrave, "Modelling polycrystalline semiconductor solar cells," *Thin Solid Films*, vol. 361, pp. 527–532, 2000.

[51] R. MacKenzie, C. Shuttle, M. Chabinyc, and J. Nelson, "Extracting microscopic device parameters from transient photocurrent measurements of p3ht: Pcbm solar cells," *Advanced Energy Materials*, vol. 2, no. 6, pp. 662–669, 2012.

[52] R. MacKenzie, T. Kirchartz, G. Dibb, and J. Nelson, "Modeling nongeminate recombination in p3ht: Pcbm solar cells," *The Journal of Physical Chemistry C*, vol. 115, no. 19, pp. 9806–9813, 2011.

[53] K. Mohammed, "Calculation of the radiative lifetime and optical properties for three-dimensional (3d) hybrid perovskites."

[54] O. Madelung, *Semiconductors: data handbook*. Springer Science & Business Media, Germany, 2012.

[55] P. Giannozzi, S. Baroni, N. Bonini, M. Calandra, R. Car, C. Cavazzoni, D. Ceresoli, G. Chiarotti, M. Cococcioni, I. Dabo, *et al.*, "Quantum espresso: a modular and open-source software project for quantum simulations of materials," *Journal of physics: Condensed matter*, vol. 21, no. 39, p. 395502, 2009.

[56] J. Perdew, K. Burke, and M. Ernzerhof, "Generalized gradient approximation made simple," *Physical review letters*, vol. 77, no. 18, p. 3865, 1996.

[57] S. Goedecker, M. Teter, and J. Hutter, "Separable dual-space gaussian pseudopotentials," *Physical Review B*, vol. 54, no. 3, p. 1703, 1996.

[58] W. Jones and N. March, *Theoretical solid state physics: Perfect lattices in equilibrium*, vol. 1. Courier Corporation, New York, 1973.

[59] P. B. Allen and B. Mikovic in *Solid State Physics* (H. Ehrenreich, F. Seitz, and D. Turnbull, eds.), vol. 37, p. 1, Academic, New York, 1982.

[60] A. Migdal, "Interaction between electrons and lattice vibrations in a normal metal," *Sov. Phys. JETP*, vol. 7, no. 6, pp. 996–1001, 1958.

[61] S. Baroni, S. de Gironcoli, A. Dal Corso, and P. Giannozzi, "Phonons and related crystal properties from density-functional perturbation theory," *Rev. Mod. Phys.*, vol. 73, no. 2, pp. 515–562, 2001.

[62] S. Y. Savrasov and D. Y. Savrasov, "Electron-phonon interactions and related physical properties of metals from linear-response theory," *Phys. Rev. B*, vol. 54, no. 23, p. 16487, 1996.

[63] F. Giustino, M. L. Cohen, and S. G. Louie, "Electron-phonon interaction using wannier functions," *Phys. Rev. B*, vol. 76, p. 165108, Oct 2007.

[64] I. Tamm, "Relativistic interaction of elementary particles," *J. Phys. USSR*, vol. 9, p. 449, 1945.

[65] S. Dancoff, "Non-adiabatic meson theory of nuclear forces," *Phys.Rev.*, vol. 78, no. 4, p. 382, 1950.

[66] C. Kittel, P. McEuen, and P. McEuen, *Introduction to solid state physics*, vol. 8. Wiley, New York, 1996.

[67] T. Trupke, M. Green, and P. Würfel, "Improving solar cell efficiencies by up-conversion of sub-band-gap light," *Journal of Applied Physics*, vol. 92, no. 7, pp. 4117–4122, 2002.

[68] J. de Wild, J. Rath, A. Meijerink, W. Van Sark, and R. Schropp, "Enhanced near-infrared response of a-si: H solar cells with β-nayf4: Yb3+ (18%), er3+ (2%) upconversion phosphors," *Solar energy materials and solar cells*, vol. 94, no. 12, pp. 2395–2398, 2010.

[69] H. Lian, Z. Hou, M. Shang, D. Geng, Y. Zhang, and J. Lin, "Rare earth ions doped phosphors for improving efficiencies of solar cells," *Energy*, vol. 57, pp. 270–283, 2013.

[70] W. Yang, X. Li, D. Chi, H. Zhang, and X. Liu, "Lanthanide-doped upconversion materials: emerging applications for photovoltaics and photocatalysis," *Nanotechnology*, vol. 25, no. 48, p. 482001, 2014.

[71] S. Fischer, H. Steinkemper, P. Löper, M. Hermle, and J. Goldschmidt, "Modeling upconversion of erbium doped microcrystals based on experimentally determined einstein coefficients," *Journal of applied physics*, vol. 111, no. 1, p. 013109, 2012.

[72] M. Vega, P. Alemany, I. Martin, and J. Llanos, "Structural properties, judd–ofelt calculations, and near infrared to visible photon upconversion in er 3+/yb 3+ doped batio 3 phosphors under excitation at 1500 nm," *RSC Advances*, vol. 7, no. 17, pp. 10529–10538, 2017.

[73] B. Zhou, E. Pun, H. Lin, D. Yang, and L. Huang, "Judd–ofelt analysis, frequency upconversion, and infrared photoluminescence of ho 3+-doped and ho 3+/yb 3+-codoped lead bismuth gallate oxide glasses," *Journal of Applied Physics*, vol. 106, no. 10, p. 103105, 2009.

[74] B. Walsh, "Judd-ofelt theory: principles and practices," in *Advances in Spectroscopy for Lasers and Sensing*, pp. 403–433, Springer, Germany, 2006.

[75] L. Shanfeng, M. Zhang, P. Yang, Q. Zhang, and Z. Mingshan, "Rate equation model analysis on the infrared and upconversion emission of er/yb co-doped borate-silicate glass," *Journal of Rare Earths*, vol. 28, no. 2, pp. 237–242, 2010.

[76] C. Strohhöfer and A. Polman, "Absorption and emission spectroscopy in er3+–yb3+ doped aluminum oxide waveguides," *Optical Materials*, vol. 21, no. 4, pp. 705–712, 2003.

[77] C. Strohhöfer and A. Polman, "Relationship between gain and yb 3+ concentration in er 3+–yb 3+ doped waveguide amplifiers," *Journal of Applied Physics*, vol. 90, no. 9, pp. 4314–4320, 2001.

[78] T. Komukai, T. Yamamoto, T. Sugawa, and Y. Miyajima, "Upconversion pumped thulium-doped fluoride fiber amplifier and laser operating at 1.47/spl mu/m," *IEEE Journal of Quantum Electronics*, vol. 31, no. 11, pp. 1880–1889, 1995.

[79] W. Yin, T. Shi, and Y. Yan, "Unique properties of halide perovskites as possible origins of the superior solar cell performance," *Advanced Materials*, vol. 26, no. 27, pp. 4653–4658, 2014.

[80] N. Jeon, J. Noh, Y. Kim, W. Yang, S. Ryu, and S. Seok, "Solvent engineering for high-performance inorganic–organic hybrid perovskite solar cells," *Nature materials*, vol. 13, no. 9, p. 897, 2014.

[81] W. Yang, J. Noh, N. Jeon, Y. Kim, S. Ryu, J. Seo, and S. Seok, "High-performance photovoltaic perovskite layers fabricated through intramolecular exchange," *Science*, vol. 348, no. 6240, pp. 1234–1237, 2015.